Journal of Applied Polymer Science

Modeling of time dependent mechanical behavior of polymers: Comparison between amorphous and semicrystalline polyethylene terephthalate

Florian Gehring,[1,2,3,4,5] Jean-Luc Bouvard,[6] Noëlle Billon[6]

[1]Normandie Univ, France
[2]UNICAEN, CIMAP UMR 6252, CAEN, F-14032, France
[3]ENSICAEN, CIMAP UMR 6252, CAEN, F-14032, France
[4]CEA, UMR 6252, CAEN, F-14032, France
[5]CNRS, UMR 6252, CAEN, F-14032, France
[6]CEMEF – Centre De Mise En Forme Des Matériaux, CNRS UMR 7635, MINES ParisTech, PSL-Research University, CS 10207 Rue Claude Daunesse 06904 Sophia Antipolis Cedex, France
Correspondence to: F. Gehring (E-mail: florian.gehring@unicaen.fr)

ABSTRACT: Revisited network theory to account for inelasticity[1,2] was used to model behavior of amorphous and semicrystalline PET. Semicrystalline materials were obtained through cold crystallization of the amorphous one making the crystalline microstructure the only difference. The model considers microstructure at a mesoscopic level through the description of an equivalent network evolving with internal state variables. Inelastic phenomena are assumed to result from the evolution of entanglements and of density of weak bond between adjacent chains (van der Walls or H-bond, etc.). The experiment data base included nonmonotonic tensile test coupled with synchronized digital image correlation and infrared measurement device for capturing the time and temperature dependence of the material. Model show a pretty good ability to reproduce time dependent behavior of the two materials. Analysis of the parameters also shows a coherent evolution with the microstructure though this latter is not explicitly accounted for in the model. Further study will make relationship between microstructure and parameters clearer. © 2016 Wiley Periodicals, Inc. J. Appl. Polym. Sci. **2016**, *133*, 43837.

KEYWORDS: mechanical properties; structure-property relations; theory and modeling; thermoplastics; viscosity and viscoelasticity

Received 22 December 2015; accepted 25 April 2016
DOI: 10.1002/app.43837

INTRODUCTION

Despite of the large number of constitutive models available in the literature (see Ref. 3 for a review), complete modeling of the mechanical behavior of thermoplastics polymers is still an open question. The nonlinearity of their behavior, even at moderate strain and the combination of viscoelastic, viscoplastic, and strain hardening (resp., softening) mechanisms without any clear thresholds make difficult the definition of a general frame. The sensibility of polymer mechanical behavior to temperature governed by discrete relaxations and its strong coupling with strain-rate dependence lead to complex evolution for parameters when metal-like or even classical approaches are used.

Moreover, often technical polymers are semicrystalline material in which strong relationship exists between microstructure and macroscopic behavior. In such a case, models have to account for the coexistence of two very different phases and for their tricky respective organization. First models are based on mixture theory that combines the behavior of crystalline and amorphous phases, whereas microstructure is much more complex than a blend of two phases and whereas role of tight molecules are known to be of prime importance. Constitutive equations were mainly proposed to account for macroscopic characteristics such as crystal volume fraction (see for instance[4–6]). Another approach is based on models consistent with continuum mechanics (among others[7–9]) in which global behavior is ruled by energy potentials and dissipation pseudo-potentials that depends on postulated internal state variables. Such models have shown a certain level of efficiency but for a limited range of conditions. Moreover, such approaches are based on "*a priori*" decomposition of experimental observations into basic components accounting for (i) reversible or irreversible mechanisms; (ii) time-dependent or independent behavior. Each component is then modeled through the combination of "simple elements" (such as spring/dashpot) that can lead to complex model.[10] In finite strain formulation Ayoub *et al.*[11] adopted and

extended the physically—based elastic—viscoplastic model proposed by Boyce *et al.*[12] and Ahzi *et al.*[13] to develop model describing the mechanical behavior of semicrystalline polymers. In their formalism, the inelastic mechanisms involve a visco-hyperelastic network resistance acting in parallel with a visco-elastic–intermolecular resistance assumed to be the contribution of an amorphous and a crystalline phase.

Others authors used internal state variables theory to build model in which internal variables are hoped to be physically motivated and associated to physical microstructural features see for instance the work of Refs. 14–16 or the work of Dusunceli and Colak[17] in which they modified, the small strain, isotropic, viscoplasticity theory based on overstress[18,19] to simulate viscous behavior. The authors considered the polymeric materials as a composite material taking into account the crystallinity ratio. However, this latter description is generally over-simplified due to its complexity and, whatever this description, lack of knowledge of mechanical behavior of each phase remain making global modeling uncertain.

Some authors used the mean field mechanical approach to obtain the effective properties of polymer through homogenization[20–22] to mention few. Referring to a study by Arnoult *et al.*[23] and Guegen *et al.*,[24] they proposed a three-phase model to estimate the effective properties of PET. The model consisted of an ellipsoidal inclusion consisting of three domains (crystalline lamella, rigid amorphous phase or interphase region, and mobile amorphous phase) embedded in a reference homogeneous medium.

Recent proposal by Billon[1] focused on potential alternative route for constitutive equations to model time-dependent mechanical behavior of polymers, whose efficiency was first tested on amorphous material above T_g. Basic idea was to start with the fact that polymers are covalent chains and that presumably this should impact or control most of their properties (at least above T_g). So the central component of modeling concept should be a polymer-like component rather than elastic spring or dashpot. Statistical network was chosen. Inelastic phenomenon could have been introduced either through "visco-like" elements or pseudo dissipation potentials (as already proposed see Ref. 1 for some examples). However, hoping reducing the number of parameters it was suggested that these later could result from changes in microstructure accounted for through the evolution of associated state variables. As from a physical point of view strain-rate sensitivity is not the cause of viscoelasticity but is the consequence of physical process (here microstructure re-arrangement) depending on time through intrinsic kinetics, effort was put in introducing this kinetics in the model. So the polymer is assumed to have the same behavior as an equivalent statistical network modified to account for the effect of microstructure evolutions which promote inelastic processes in the polymer. The non-Gaussian statistical approach of entangled polymer network developed by Edwards and Vilgis[25] is used. The Edwards and Vilgis model is based on the Ball *et al.* theory[26] that introduces the concept of slip-link to account for the entanglement entropy.

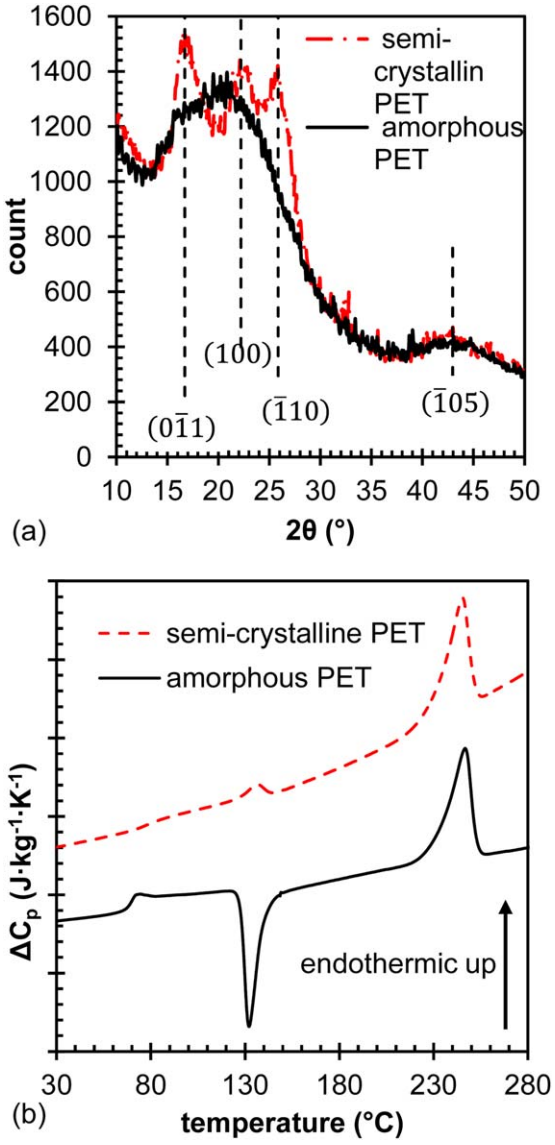

Figure 1. (a) WAXS spectra of PET sheets and (b) DSC heating thermograms at 10 °C/min (curves have been vertically shift). [Color figure can be viewed in the online issue, which is available at wileyonlinelibrary.com.]

More precisely, the model considers microstructure at a mesoscopic level through some internal variables involved in the equivalent network description. Four descriptors of internal variables rule the energy of the material by the end:

- N_c, the density of permanent crosslinks between statistical chains;
- N_s, the density of additional entanglements whose level of freedom ("tightness") results in one parameter (η in the following).
- η, which is related to the length of slippage in links;
- α, the inextensibility of the chain.

Inelastic phenomena are assumed to result from the evolution of some of those variables ruled by postulated kinetics laws. They have to be accounted for in the energy balance at any

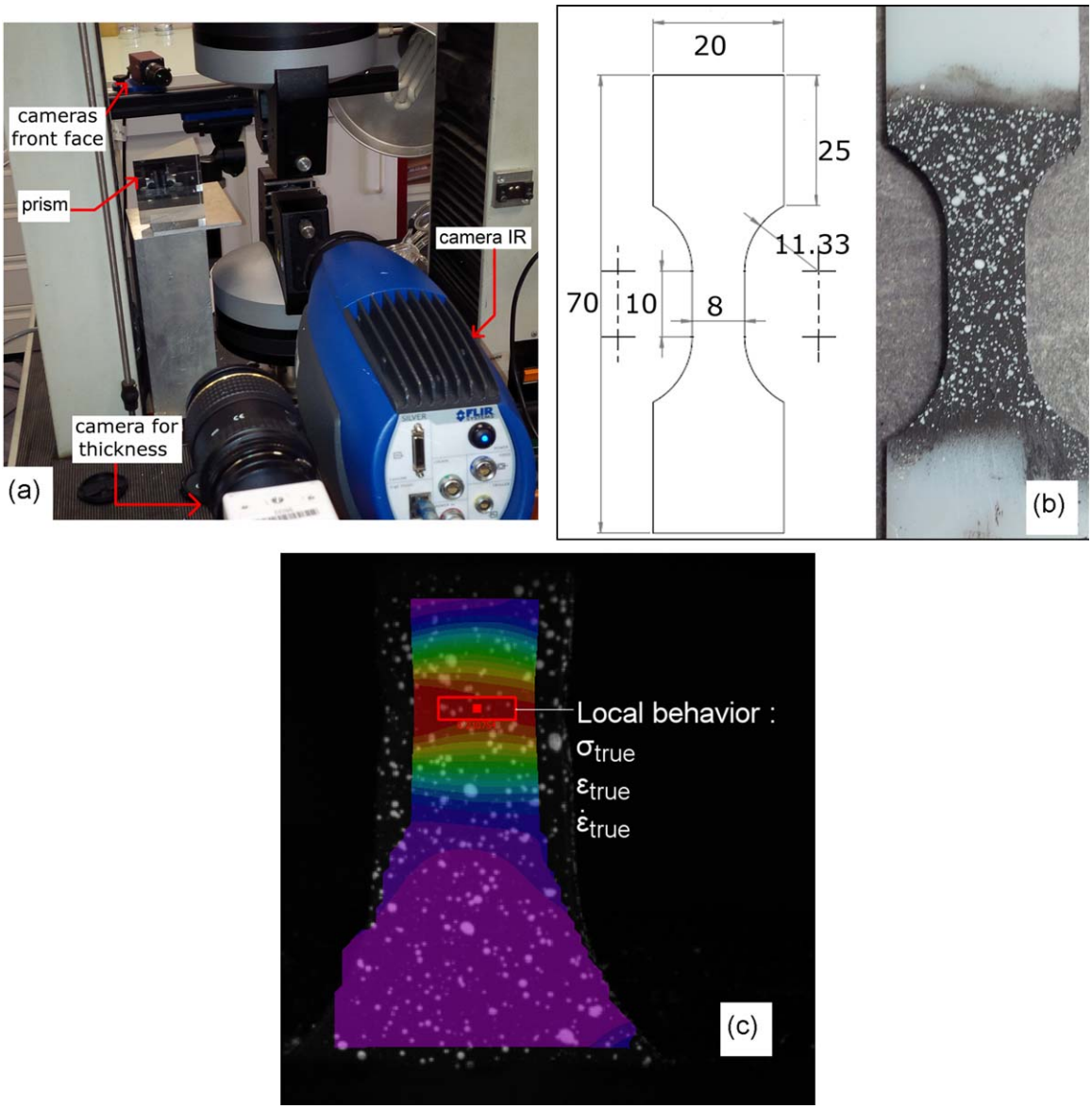

Figure 2. (a) experimental setup, (b) specimen dimensions and random pattern on the front surface, (c) true strain field and area of local behavior analyses. [Color figure can be viewed in the online issue, which is available at wileyonlinelibrary.com.]

time and associated increase in energy has to be compensated. Similarly to Griffith theory for rupture, one postulates that energy for microstructure evolution comes from the release of part of elastic energy in the bulk, which induces some inelastic strain-rate. So at any time inelastic strain rate is related to the rate of variation of the microstructure state variables. First, disentanglement of the amorphous polymer chains was associated with an increase of the slippage length in the entanglements.[1,25,26] Abbility of the 1D (one dimensional) limit of the model to reproduced most of the macroscopic viscoelastic behaviors of polymers with a reduced number of parameters was illustrated.[1] Feasibility to model rubbery PMMA over a wide range of strain rates and temperatures with a using equivalent strain rate at reference temperature as a "new" coupled parameter to account for temperature and strain rate coupled effects was also reported.[1] Recently, Maurel-Pantel *et al.*[2] completed the approach proposing the fully 3D writing of the resulting thermomechanical model in the rigorous frame of thermodynamics.

The 1D limit of this approach was applied with reasonable success on Polyamide 66 over a wide range of strain rate and temperature in tensile conditions. However, a precise analysis showed that agreement could be improved, especially concerning the initial "rigidity" that seemed to be under estimated (error less than 10%, nevertheless). Such underestimation could be due to a certain weakness in modeling interaction between chains that are of different type, may be especially in the crystalline zone. Keeping the same mesoscopic level of description Billon *et al.*[27] suggested to enrich the model by adding one network branch to account for weak interaction (van der Walls, H-bonds, or so on), additionally to entanglements.

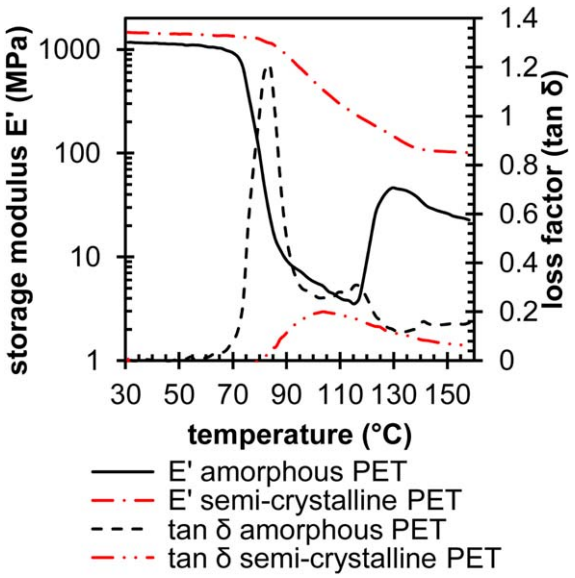

Figure 3. Temperature scans from 30 to 160 °C at 1 Hz for the amorphous (black) and semicrystalline (red) PET. [Color figure can be viewed in the online issue, which is available at wileyonlinelibrary.com.]

In this article, this enrichment is described and validated. As crystal may be a tricky point to account for through such approach PET is chosen as this material can be obtained either in an amorphous or in a semicrystalline state keeping processing unchanged by cooling and annealing protocol. Our focus is to examine the influence of the mechanical behavior induced by the amorphous or the semicrystalline microstructure on the evolution of internal variables to assess their physical meanings.

The article proceeds first by an overview of the mechanical behavior of an amorphous PET and a cold crystallized PET tested under several strain rates and tensile conditions (load-unload and load-relax-unload-relax). Next, the 3D thermomechanical formalism of the model is reminded and its extension is presented. Constitutive equations of the model accounting for several microstructure rearrangements (disentanglement and loss of connectivity) contributions are described within the large deformation formalism and follows the thermodynamic framework. In constitutive modeling section, an inverse identification procedure for the parameters of the model and their validation are described. The description of equivalent chain network of semicrystalline and amorphous polymer is discussed. Finally, conclusions are drawn.

EXPERIMENTAL

Material and Methods

A PET resins for ISBM (Injection Stretch Blow Moulding) currently known as "Invista 1101" with an intrinsic viscosity (IV) of 0.83 dL/g was used. It was supplied as amorphous plaques of 80 mm by 80 mm dimensions and 2.1 mm thickness. Material was kept amorphous thanks to injection molding in a cold mold according to the state of the art. Some of the plaques were postcrystallized during isothermal annealing above glass transition temperature under hydraulic laboratory press. Applying a temperature of 115 °C during 2 h was found to be enough to reach a stable crystallization state without any degradation or hydrolysis. To account for relaxation involved in that treatment, amorphous plaques were also annealed at 80 °C for 1 h. This treatment was able to "renew" PET, that is, counterbalance physical aging of PET[28] and relax residual stresses due to processing. All tested specimens were further machined parallel to the injection flow.

Wide-angle X-ray θ–2 θ diffraction scans in reflection were performed using Cu Kα 1.54 Å. As shown in Figure 1(a), broad peaks of low intensity were found for PET after cold crystallization that corresponded to the classical triclinic structure of PET[29] whereas amorphous materials only exhibited an amorphous diffusion.

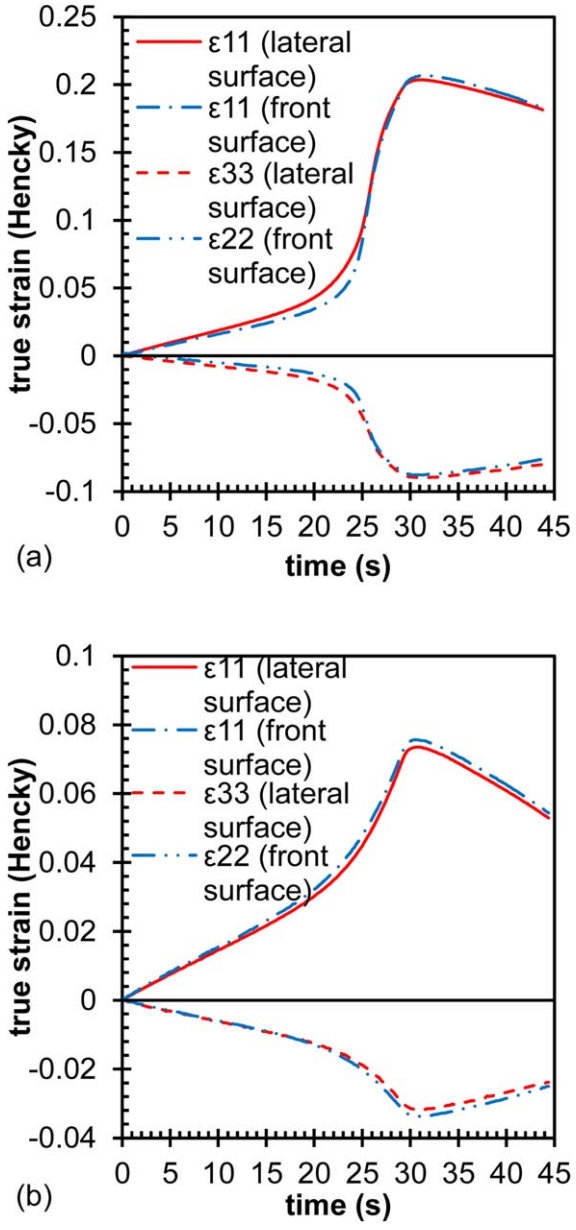

Figure 4. Strain components computed to ensure transversally isotropic behavior of (a) amorphous PET and (b) semicrystalline PET. [Color figure can be viewed in the online issue, which is available at wileyonlinelibrary.com.]

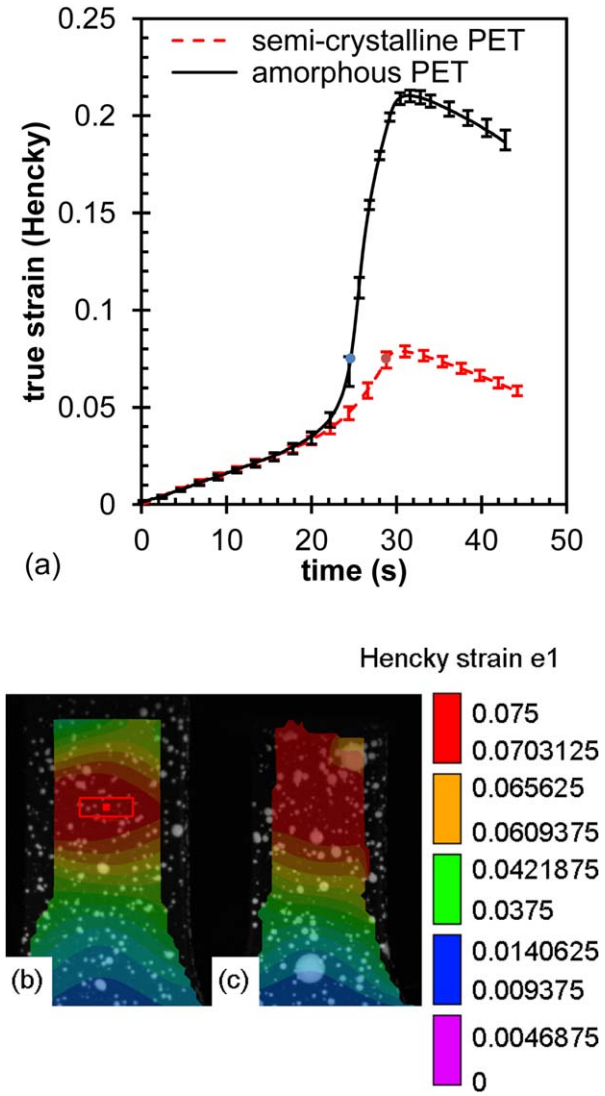

Figure 5. (a) Evolution of strain versus time during uploading and unloading tensile test at an initial strain rate of $2 \cdot 10^{-3}s^{-1}$; (b) principal strain field at local maximum local strain of 0.075 for amorphous PET; and (c) principal strain field at local maximum local strain of 0.075 for semicrystalline PET. [Color figure can be viewed in the online issue, which is available at wileyonlinelibrary.com.]

Broadness of diffraction peak for semicrystalline PET suggests that lamellae should be small or imperfect.

DSC measurements were performed on less than 10 mg weight and 200 μm-thick disk shaped samples tooled from the plaques (close to the surface). This geometry ensured a good thermal contact in the DSC machine for a maximum accuracy of measurements. Heating rate was 10 °C/min from 30 to 280 °C. Indeed, amorphous PET had to be as amorphous as possible after rejuvenating and the treatment time for PET subjected to cold crystallization has to be long enough to achieve complete transformation of the crystalline domains.

Amorphous PET exhibited a classical trace for this type of material with three transitions [Figure 1(b)]: T_g at 75 °C, an exothermic crystallization peak at 132 °C and the fusion at 246 °C. Crystallization enthalpy (−32 J/g) was almost equal to the fusion enthalpy, which confirmed that initial plaque was amorphous as suggested by X-ray diffraction [Figure 1(a)]. Postcrystallized PET was found not to additionally crystallize during DSC measurement. From fusion enthalpy a 31% crystallinity in mass was determined (theoretical enthalpy was taken at 120 J/g according to Ref. 30).

Polarized optical microscopy was also used attempting to address spherulitic microstructure. As a matter of fact if spherulite exists, their diameter should be less than 10 μm. However, plaques appeared to be optically uniform suggesting that polymer was homogeneous.

To summarize, amorphous PET was rejuvenated but remained amorphous whereas the semicrystalline PET was a 31% in mass crystalline material.

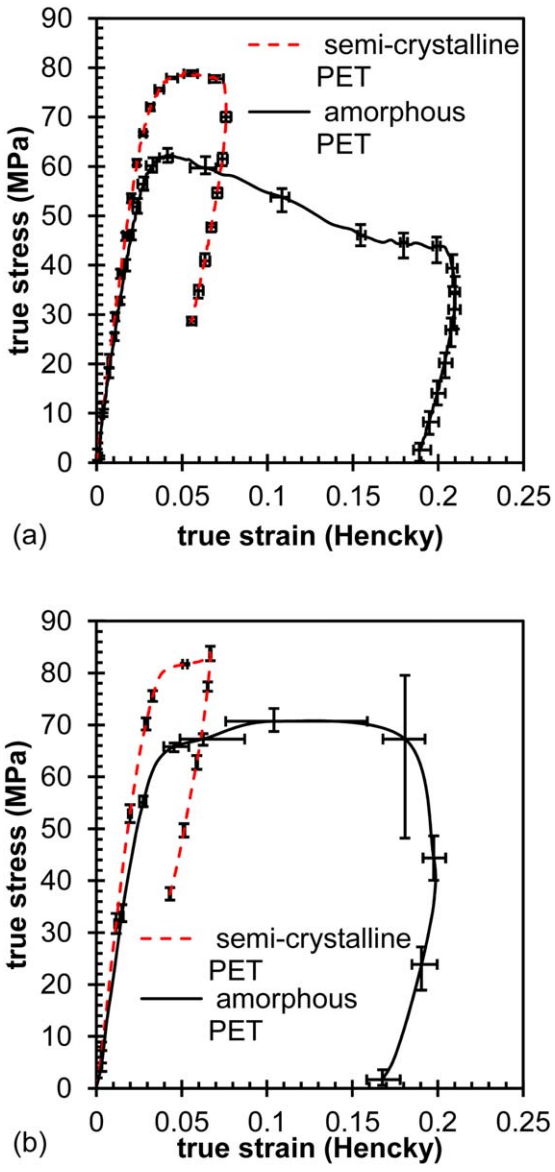

Figure 6. Uploading and unloading true stress-true strain curves obtained at initial strain rate of (a) $2 \cdot 10^{-3}s^{-1}$ and (b) $2 \cdot 10^{-2}s^{-1}$. [Color figure can be viewed in the online issue, which is available at wileyonlinelibrary.com.]

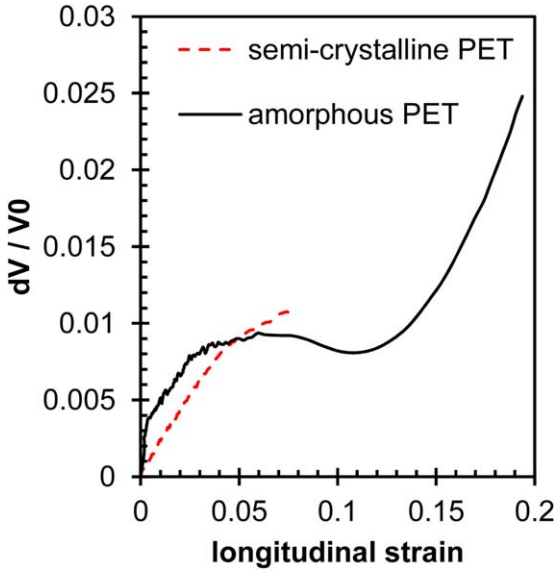

Figure 7. Volume change obtained during uniaxial tensile test at initial strain rate of $2 \cdot 10^{-3}s^{-1}$. [Color figure can be viewed in the online issue, which is available at wileyonlinelibrary.com.]

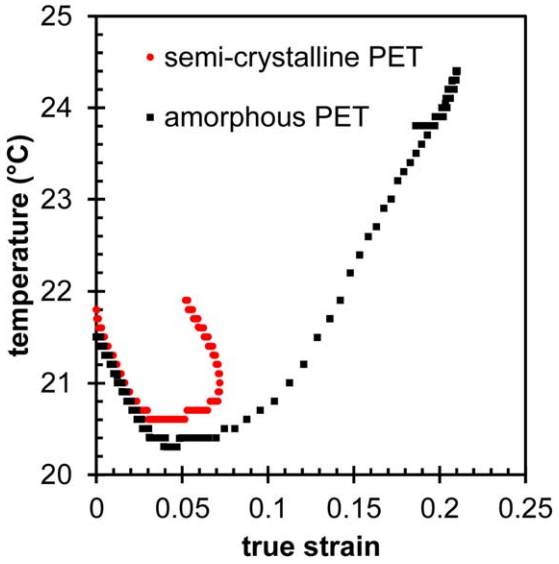

Figure 8. Temperature evolution at the necking point for uploading and unloading at initial strain rate of $2 \cdot 10^{-3}s^{-1}$. [Color figure can be viewed in the online issue, which is available at wileyonlinelibrary.com.]

DMA analyses, Triton Tritec 2000 equipment, were also performed for addressing the relaxations of the two materials. It was performed in tension on 5 mm × 3 mm rectangle-shape specimens of 2.1 mm in thickness. A maximal applied strain of 10^{-3} was chosen to guarantee the linear viscoelasticity of the material through the investigated temperature range. The heating rate was equal to 2 °C/min.

In a second step, tensile behavior at several strain rates was explored at 23 °C and at a relative humidity of 50% using an Instron electromechanical load frame after the sample have been stabilized in term of water content. The experimental setup is presented on Figure 2(a). Local strains were measured using full field measurement based on random pattern painted on surface [Figure 2(b)]. To capture the out-of-plane motion, two cameras in stereo-correlation were used to measure the displacement field on the front face surface of the sample. Using a third camera and a mirror, strain field was analyzed on the lateral surface too. Therefore, no assumption was made about the isotropy or incompressibility of the material. Our observations were focused on investigating the deformation of the gage zone as this region should stay reasonably homogenous during the tensile test. Local true stress, true strain and local true strain rate were then computed [Figure 2(c)]. Local true strain rate was not constant but known at any time. Temperature evolution on the specimen back surface was captured using infrared camera. Entire experimental database consists in performing complex loading at different strain rates (load-unload and relaxation tests). All tests were repeated at least three times. Only the average results are presented here. Estimations of errors in strain and stress measurements were added to the figures.

Viscoelasticity

The α-transition temperature (chosen at the maximum value of loss angle) for amorphous PET ranged from 75 to 89 °C for loading frequency ranging from 0.1 to 10 Hz (84 °C at 1 Hz). The α-transition temperature moved to higher temperatures for semicrystalline PET. It ranged from 90 to 103 °C for loading frequency ranging from 0.1 to 10 Hz (100 °C at 1 Hz). As expected, the drop in modulus for the semicrystalline PET is less than the amorphous one due to the presence of a crystalline structure. Moreover, the storage modulus at low temperature is slightly affected by the crystallization (Figure 3).

Crystallization of amorphous material is also visible with the increase in storage modulus close to 120 °C, which is in agreement with DSC trace if the differences in heating rates are accounted for.

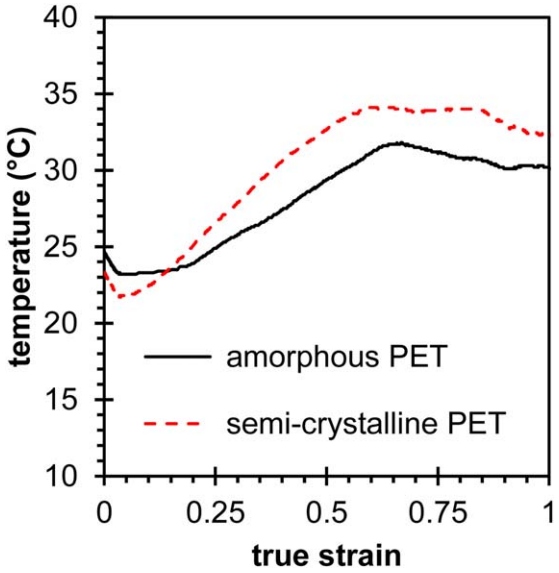

Figure 9. Temperature evolution at the necking point for monotonic tensile tests at initial strain rate of $2 \cdot 10^{-3}s^{-1}$ for the two polymers. [Color figure can be viewed in the online issue, which is available at wileyonlinelibrary.com.]

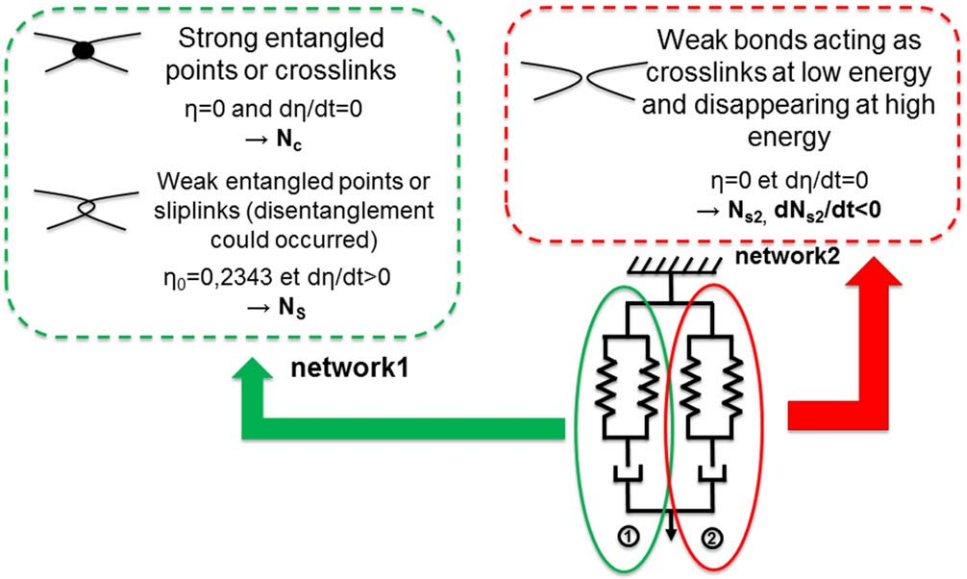

Figure 10. Schematic representation of chains interaction responsible for microstructure reorganization. [Color figure can be viewed in the online issue, which is available at wileyonlinelibrary.com.]

From this analysis, one can concluded that at 23 °C the two materials will be such that amorphous phase is its glassy state with a very low E'' modulus, making the presence of crystal their main difference.

Nevertheless the slightly postponed α transition for the semicrystalline polymer can suggest the presence of more "constrained" amorphous phase in the semicrystalline material (shorter free length, linked amorphous or so on).

Effect of the Amorphous and Semicrystalline State of PET on the Mechanical Properties

Uploading-unloading tests were used to assess inelasticity in PET at large strain for several strain rates. In this study, only crosshead velocity were controlled, which mean that strain rate varied during tension as a function of necking (Figure 4). However, exact instantaneous local strain rates were used in the parameters identification process. The crosshead velocities of 0.05 mm/s and 0.5 mm/s were selected to obtain initial strain rate of approximately $2 \cdot 10^{-3} s^{-1}$ and $2 \cdot 10^{-2} s^{-1}$, respectively. As we mentioned before, we used three cameras to capture the three main strain components. Strain components were computed by averaging strain field obtained by digital image correlation in one section of the sample process zone [zone of interest is displayed by the rectangular area in Figure 5(b)]. In the following, ε_{11} stands for the longitudinal strain, ε_{22} and ε_{33} stand for the width and thickness transverse strain, respectively. Longitudinal strain was computed on front and lateral surface to be compared and to validate the alignment and the calibration of cameras. For both materials, the strain measured in the thickness is equal to the strain measured in the specimen width (Figure 4). Therefore, amorphous and semicrystalline PET could be assumed to be transversely isotropic.

An increase in the strain rate was also observed in both materials when necking occurred [Figure 5(a)]. Principal strain field

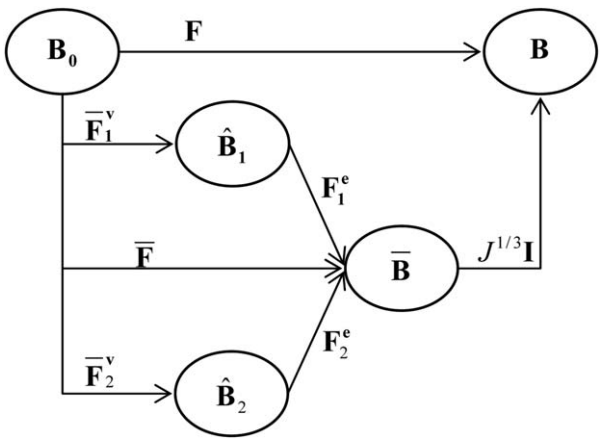

Figure 11. Schematic representation of the decomposition of the total deformation gradient.

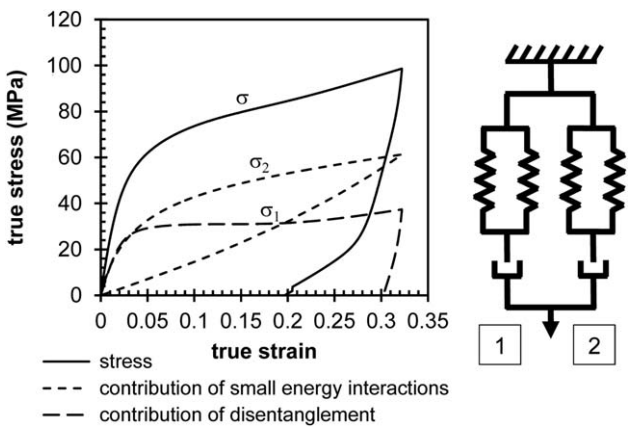

Figure 12. Contribution of chain interactions on stress-strain curves obtained for uniaxial tensile test.

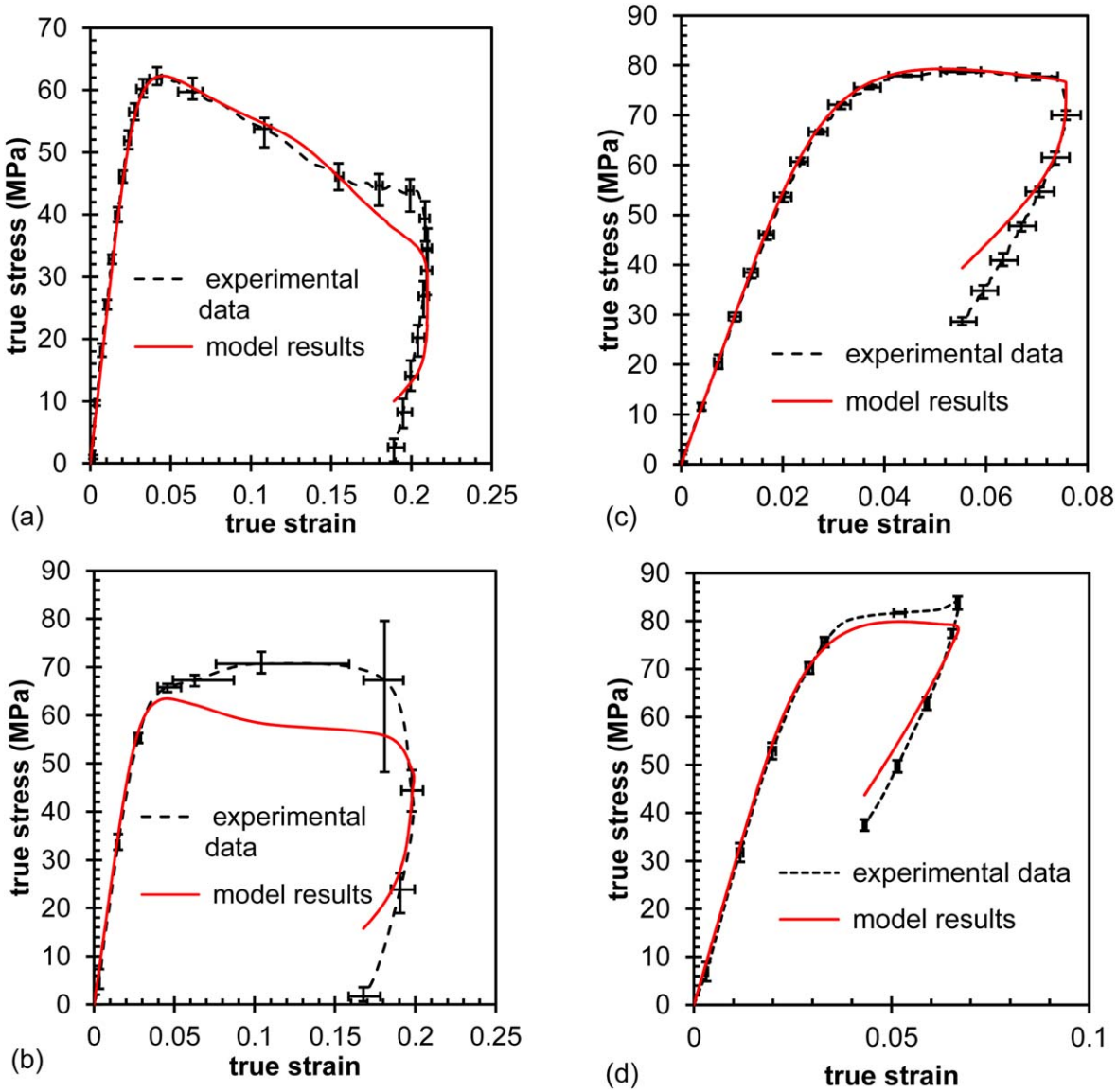

Figure 13. Comparison model-experimental for the amorphous PET at initial strain rate of (a) $2 \cdot 10^{-3}s^{-1}$ and (b) $2 \cdot 10^{-2}s^{-1}$ and for the semicrystalline PET at initial strain rate of (c) $2 \cdot 10^{-3}s^{-1}$ and (d) $2 \cdot 10^{-2}s^{-1}$. [Color figure can be viewed in the online issue, which is available at wileyonlinelibrary.com.]

obtained at the same level of local strain is given for the amorphous PET [Figure 5(b)] and for the semicrystalline PET [Figure 5(c)]. Strain was highly localized in the amorphous PET but in contrast with the semicrystalline material, strain field looks more uniform. Moreover, the out-of plane displacement at the necking onset for the amorphous PET was higher than for the semicrystalline one. As the necking in the amorphous PET was more prominent than in the semicrystalline polymer, the strain rate during necking was higher for the amorphous PET.

The true stress–true strain curves were plotted in Figure 6. Regardless the explored strain rate, the initial modulus of semicrystalline PET was only slightly higher than the modulus of amorphous PET. In accordance with DMA analyses (Figure 3), crystalline domains, obtained by cold crystallization, have small contribution to initial elastic properties. However, if one considers the nonlinear initial loading zone, rigidity of semicrystalline material appears to be more significantly greater especially at higher strain rate. The Poisson ratio was found to be close to 0.45 in both materials (0.455 for amorphous PET and 0.445 for semicrystalline PET). Indeed, as generally observed,[31] the apparent yield stress in semicrystalline PET was higher than for the one of the amorphous one. This illustrates the fact that, if exists, plastic like deformation of amorphous phase requires a higher stress to be initiated in the semicrystalline polymer which is consistent with an re-arrangement of amorphous phase due to crystallization. Some processes are still possible in the totally amorphous material that induce "plasticity" at lower stress. Obviously crystalline process will also participate to yield stress in semicrystalline polymer.

The volume change in both materials was examined. The ratio of volume change during loading is given by eq. (1):

$$\frac{dV}{V_0}=\exp(\varepsilon_1+\varepsilon_2+\varepsilon_3)-1 \quad (1)$$

where V_0 is the initial volume, $dV=(V-V_0)$ is the volume change and ε_i are the principal strains. The volume was found to increase with longitudinal strain in both materials (Figure 7). Nevertheless, the value obtained was less than 3% at a strain close to 0.2, which is coherent with a close to 0.5 Poisson ratio in the "elastic zone" and which suggest that no specific damage occurred at higher strain

Temperature evolutions were investigated for these uploading/unloading solicitations (Figure 8). Initial thermo elastic coupling could be evidenced with a 1.5° decrease in temperature. From strain of between 3 and 5% dissipation became important enough for temperature of both materials to increase. However, this increase was less than 2 °C, which allows concluding that yield that appears close to strain of 5% can be related to inelastic phenomena the initiation of which is not clear but not by self-heating as DMA proved that effect of temperature can be neglected in that range.

Amorphous phase exhibit a more important cooling effect. In this zone, strain rate are equivalent for both the two materials. So despite of a lower apparent yield stress amorphous material could involve more elastic processes than semicrystalline polymers. Concerning heat dissipation, it is also of interest to note that the more rapidly loaded amorphous material appears to heat up slower than the less rapidly loaded semicrystalline material. However, differences are so low that it would be dangerous to speculate further.

Hence, monotonic tensile tests were also performed under the same condition on larger strain levels (more than 1). At equivalent strain and strain rate, the increase in temperature is higher for the semicrystalline PET than for the amorphous one (Figure 9). Let's then conclude that processes involved in the two materials could have different natures.

Therefore, more energy seems to be dissipated in the semicrystalline PET. The reason is not obvious. Nevertheless, let us assume two different hypotheses. In one hand, the plastic dissipation of crystalline domains is added to the associated viscoelasticity of the amorphous phase leading to an increase of total dissipation. Crystalline structures are reorganized or destroyed to create new crystalline regions by external loading. In another hand, the amorphous domains that have been confined by crystal growth during crystallization may dissipate more than "the free amorphous domains." No evidence was found to confirm one of those assumptions, the truth is leading somewhere between.

CONSTITUTIVE MODELING

According to chosen model[1,2] Edwards and Vilgis' model was chosen as equivalent network. Inelastic processes were assumed to result from kinetics of internal variables variation induced by the microstructure changes under loading. In this mesoscopic approach, these mechanisms are neither amorphous nor crystalline *per se*. They are induced by the interactions between statistical chains. As displayed in Figure 10, three main interactions are considered. First, chains can be linked by permanent nodes or tight entanglements. Let's N_c be the volume density of such nodes. In parallel, other chains can be entangled, that is, connected through zones where a certain level of conformational freedom exists. Edward Vilgis used the slipping ring concept introduced by Ball.[26] Those entanglements are represented by a density N_s and their level of freedom results in one parameter, named η. If η is zero, the node is constrained and therefore equivalent to a permanent crosslink node. If η is higher than zero, chains can slip and entanglement are supposed to gain in freedom. Following previous work, the inelasticity in amorphous phase is assumed to be related to this increase of freedom in the entanglement nodes that results in an increase of η as a function of the stored elastic energy (the more energy the more rapid the disentanglement).

A third type of interaction has to be considered, which is represented by weak bonds between adjacent chains (van der Walls or H-bond, etc.). Those interactions are assumed to constrain the chain mobility up to a certain level of energy were the bond can be broken. This interaction does not have any possible "slippage" *per se* but they can disappear or be restored as a function of strain stress and/or energy. They are accounted for by a second set of crosslink nodes represented by N_{s2} where the initial density of can decrease and disappear according to a kinetics law. These interactions are assumed to be predominant in denser zones such as organized amorphous or crystal.

The three different contributions are set into two parallel branches (Figure 10). One branch represents the initial model and combines the entanglements and the permanent nodes whereas the second branch only concerns weak interactions.

Both the two branches obey to the initial concept considering that the evolution in variables is compensated by releasing stored elastic strain. The released stored energy is the source of inelasticity that is defined branch per branch. The last variables to set are the two chain extensibilities (one per branch). In the first branch representing the initial model, the chain extensibility is assumed to be constant and therefore is set as a model parameter. As far as the second branch is concerned, the chain extensibility and the level of connectivity in the chain network must be correlated. This is why we consider α^2 to be proportional to N_{s2} (disentanglement) at any time.

The Kinetics law of η and N_{s2} are defined as a function of the stored elastic energy in each branch. Then, according to previous work, mechanical problem can be written in a fully 3D form.

Kinematics

The kinematics of the problem is based on a multiplicative decomposition of the deformation gradient. Considering X an arbitrary material point in B_0 (essentially, a body is identified within a space with a fixed reference configuration), the motion of B is described through the mapping $x=y(X,t)$ via a deformation gradient (F), velocity (v), and velocity gradient (l) such as

$$F=\nabla y,\ \ v=\dot{y},\ \ l=\text{grad}\ v=\dot{F}F^{-1} \quad (2)$$

Following Flory[32] and Simo *et al.*,[33] we decompose the total deformation gradient me into uncoupled, volumetric/deviatoric

parts. For this purpose, we introduce the following volumetric/deviatoric multiplicative split of $\bar{F}$

$$F=J^{1/3}\bar{F},\ \det\bar{F}=1,\ \det F=J\ (J>0) \tag{3}$$

Following Lee,[34] Sidoroff,[35] Lubliner,[36] and more recently Andriyana *et al.*,[37] we consider a multiplicative decomposition of the volume-preserving deformation gradient $\bar{F}$ into elastic and inelastic components for each branch,

$$\bar{F}=\bar{F}_1^e\bar{F}_1^v=\bar{F}_2^e\bar{F}_2^v \tag{4}$$

where $\left(\bar{F}_k^e\right)_{k=\{1,2\}}$ represents the elastic part due to "reversible elastic mechanisms," such as chain rotation inducing the different conformations of the intermolecular structure in polymeric material. $\left(\bar{F}_k^v\right)_{k=\{1,2\}}$ represents the inelastic part due to the intermolecular interaction between chains inducing a reorganization of the polymer network under deformation.

Figure 11 summarizes the decomposition described in eqs. (3) and (4) into the different configurations.

The following Cauchy Green tensors and velocity gradients are written using eqs. (3) and (4)

$$C=F^TF=J^{2/3}\bar{C},\ \bar{C}=\bar{F}^T\bar{F},\ J=(\det\ C)^{1/2} \tag{5}$$

$$\bar{C}_k^e=\bar{F}_k^{eT}\bar{F}_k^e=\left(\bar{F}_k^v\right)^{-T}\bar{C}\left(\bar{F}_k^v\right)^{-1},\ k=\{1,2\} \tag{6}$$

$$\bar{L}=\bar{L}_k^e+\bar{F}_k^e\bar{L}_k^v\bar{F}_k^{e-1},\ k=\{1,2\} \tag{7}$$

where

$$\bar{L}_k^v=\dot{\bar{F}}_k^v\bar{F}_k^{v-1},\ k=\{1,2\} \tag{8}$$

The velocity gradients can be decomposed into their symmetric and skew parts, for example, $\bar{L}=\bar{D}+\bar{W}$, with $\bar{D}=\mathrm{sym}(\bar{L})$ and $\bar{W}=\mathrm{skew}(\bar{L})$. Assuming that the flow is irrotational, we have $\bar{W}_1^v=\bar{W}_2^v=0$, and therefore the velocity gradients in eq. (7) can be expressed as: $\bar{L}_1^v=\bar{D}_1^v$, $\bar{L}_2^v=\bar{D}_2^v$

Classically, the Cauchy stress can be written as

$$\sigma=J^{-1}\tau=J^{-1}\mathrm{FSF}^T \tag{9}$$

where τ is the Kirchhof stress and S is the second Piola–Kirchhoff stress expressed in configuration B_0. S will be determined from the thermodynamic framework described in the next section.

Thermodynamics

The internal dissipation inequality can be obtained from the second law of thermodynamic and is given by:

$$S:\frac{1}{2}\dot{C}-\dot{\psi}\geq 0 \tag{10}$$

where ψ is the Helmholtz free energy per unit volume.

The Helmholtz free energy function is assumed to depend on a number of state variables: the elastic Cauchy–Green tensor $\left(\bar{C}_k^e\right)_{k=\{1,2\}}$ and a set of ISVs $\bar{\Pi}$, as

$$\psi_v=\psi_v\left[\left(\bar{C}_k^e\right)_{k=\{1,2\}},\bar{\Pi}\right] \tag{11}$$

A special form of the free energy based on the non-Gaussian statistic approach of polymer network developed by Edwards and Vilgis[25] and extended by Refs. 1 and 38 is chosen in this study. The free energy can be decomposed into two components: (i) the energy due to the polymer network deformation restrained by permanent nodes (crosslinks); and (ii) the energy due to the polymer network deformation restrained by slip links such as entanglement points. The Edwards and Vilgis hyperelastic model can therefore be described by:

$$\psi\left(\bar{C}^e,\eta,\theta\right)=(1/2)k\theta\left[N_c\psi_c\left(\bar{C}^e,\alpha\right)+N_s\psi_s\left(\bar{\mathbf{C}}^{\mathbf{e}},\eta\right)\right] \tag{12}$$

where k is the Boltzmann's constant; θ is the temperature; N_c is the density per unit volume of crosslinking; N_s is the density per unit volume of entanglement points; α is the limit of chain extensiblity. N_s and N_c are usually given in 10^{25} m^{-3}. In the following,

In the case of isothermal testing, the free energy described in eq. (11) can now be specialized to:

$$\psi_v=\sum_{k=1}^{2}\bar{\psi}_v^k\left(\bar{C}_k^e,\bar{\eta}_k,N_s^k,\bar{\alpha}_k\right)+\hat{\bar{\psi}}_J(J) \tag{13}$$

where $\bar{\psi}_v^k$ represents the isochoric contribution of the branch k to the free energy ψ_v and $\hat{\bar{\psi}}_J(J)$ represents the volumetric functional form introduced by Ref. 39.

Thus, the time derivative of ψ_v can be computed as

$$\dot{\psi}_v=\sum_{k=1}^{2}\left(\frac{\partial\bar{\psi}_v^k}{\partial\bar{C}_k^e}:\dot{\bar{C}}_k^e+\frac{\partial\bar{\psi}_v^k}{\partial\bar{\eta}_k}\dot{\bar{\eta}}_k+\frac{\partial\bar{\psi}_v^k}{\partial N_s^k}\dot{N}_s^k+\frac{\partial\bar{\psi}_v^k}{\partial\bar{\alpha}_k}\dot{\bar{\alpha}}_k\right)+\frac{\partial\hat{\bar{\psi}}_J(J)}{\partial J}\dot{J} \tag{14}$$

Guided by Reese and Govindjee,[40] Simo and Hughes,[39] Holzapfel,[41] the first term of eq. (14) can be evaluated as

$$\begin{aligned}\frac{\partial\bar{\psi}_v^k}{\partial\bar{C}_k^e}:\dot{\bar{C}}_k^e&=\frac{\partial\bar{\psi}_v^k}{\partial\bar{C}_k^e}:\left[-L_k^{vT}\bar{C}_k^e+\left(F_k^v\right)^{-T}\dot{\bar{C}}\left(F_k^v\right)^{-1}-\bar{C}_k^eL_k^v\right]\\&=\left(F_k^v\right)^{-1}\left(\frac{\partial\bar{\psi}_v^k}{\partial\bar{C}_k^e}\right)\left(F_k^v\right)^{-T}:\dot{\bar{C}}-\bar{C}_k^e\left(2\frac{\partial\bar{\psi}_v^k}{\partial\bar{C}_k^e}\right):\bar{D}_k^v\end{aligned} \tag{15}$$

where we have used eq. (6) and the symmetry of $\bar{C}_k^e$, $\frac{\partial\bar{\psi}_v^k}{\partial\bar{C}_k^e}$, $\bar{D}_k^v$.

Moreover from eq. (5), we have[40,41]

$$\dot{\bar{C}}=\mathbf{2}\left(\frac{\partial\bar{C}}{\partial C}\right):\frac{1}{2}\dot{C}=2J^{-2/3}\mathrm{P}^T:\frac{1}{2}\dot{C},\ \dot{J}=JC^{-1}:\frac{1}{2}\dot{C} \tag{16}$$

$$\mathrm{P}^T=\mathrm{I}-\frac{1}{3}C\otimes C^{-1} \tag{17}$$

Substituting eq. (14) together with eqs. (15) and (16) into the dissipation inequality, eq. (10), we obtain

$$\begin{aligned}&\left\{S-J^{-2/3}\mathrm{DEV}\left[\sum_{k=1}^{2}\left(F_k^v\right)^{-1}\left(2\frac{\partial\bar{\psi}_v^k}{\partial\bar{C}_k^e}\right)\left(F_k^v\right)^{-T}\right]-\frac{\partial\hat{\bar{\psi}}_J(J)}{\partial J}JC^{-1}\right\}:\frac{1}{2}\dot{C}\\&+\sum_{k=1}^{2}\left[\bar{C}_k^e\sum\left(2\frac{\partial\bar{\psi}_v^k}{\partial\bar{C}_k^e}\right):\bar{D}_k^v-\left(\frac{\partial\bar{\psi}_v^k}{\partial\bar{\eta}_k}\dot{\bar{\eta}}_k\right)-\left(\frac{\partial\bar{\psi}_v^k}{\partial N_s^k}\dot{N}_s^k\right)-\left(\frac{\partial\bar{\psi}_v^k}{\partial\bar{\alpha}_k}\dot{\bar{\alpha}}_k\right)\right]\geq 0\end{aligned} \tag{18}$$

with

$$\mathbf{DEV}(\bullet)=(\bullet)-\frac{\mathbf{1}}{\mathbf{3}}[(\bullet):\mathrm{C}]C^{-1} \tag{19}$$

Using standard arguments,[42] we obtain from eq. (18) the constitutive equation of S,

$$S=J^{-2/3}\mathbf{DEV}(\bar{S})+pJC^{-1} \tag{20}$$

with

$$\bar{S}=\sum_{k=1}^{2}(F_k^v)^{-1}\left(2\frac{\partial\bar{\psi}_v^k}{\partial\bar{C}_k^e}\right)(F_k^v)^{-T},\ p=\frac{\partial\hat{\bar{\psi}}_J(J)}{\partial J} \tag{21}$$

The dissipation inequality is then

$$\sum_{k=1}^{2}\left[\bar{C}_k^e\sum\left(2\frac{\partial\bar{\psi}_v^k}{\partial\bar{C}_k^e}\right):\bar{D}_k^v-\left(\frac{\partial\bar{\psi}_v^k}{\partial\bar{\eta}_k}\dot{\bar{\eta}}_k\right)-\left(\frac{\partial\bar{\psi}_v^k}{\partial N_s^k}\dot{N}_s^k\right)-\left(\frac{\partial\bar{\psi}_v^k}{\partial\bar{\alpha}_k}\dot{\bar{\alpha}}_k\right)\right]\geq 0 \tag{22}$$

Introducing for each branch the Mandel stress, $\bar{M}_k=\bar{C}_k^e\left(2\frac{\partial\bar{\psi}_v^k}{\partial\bar{C}_k^e}\right)$, we have

$$\underbrace{\bar{M}_k:\bar{D}_k^v}_{\text{inelastic dissipation}}\ \underbrace{-\left(\frac{\partial\bar{\psi}_v^k}{\partial\bar{\eta}_k}\dot{\bar{\eta}}_k+\frac{\partial\bar{\psi}_v^k}{\partial N_s^k}\dot{N}_s^k+\frac{\partial\bar{\psi}_v^k}{\partial\bar{\alpha}_k}\dot{\bar{\alpha}}_k\right)}_{\text{internalwork}}\geq 0,\ k=\{1,2\} \tag{23}$$

where the first term represents the inelastic work dissipated from reversible ($k=1$) and irreversible ($k=2$) mechanisms associated with the polymer network reorganization (chains relaxation inducing chains disentanglement) and the internal work associated with the field of residual microstresses induced by entanglements points, crystallized regions, and chain alignment.

Constitutive Model

This section develops in detail the 3D model equations describing the mechanical behavior of the polymer.

To determine the Cauchy stress tensor σ, we use the additive split of the Helmholtz free energy described in eq. (13). We need now to specialize the expression of the isochoric and volumetric parts of the free energy.

The energy of Edward and Vilgis described in eq. (12) can be written as a function of the invariants $(\bar{I}_1^k,\bar{I}_2^k,\bar{I}_3^k)$:

$$\bar{\psi}_v^k(\bar{I}_1^k,\bar{I}_2^k,\bar{I}_3^k,\bar{\eta}_k,\bar{\alpha}_k)=(1/2)k\theta\left[\begin{array}{l}\underbrace{N_c^k\left(\frac{(1-\bar{\alpha}_k^2)\bar{I}_1^e}{(1-\bar{\alpha}_k^2\bar{I}_1^e)}+\ln(1-\bar{\alpha}_k^2\bar{I}_1^e)\right)}_{w_c^k}\\ \underbrace{+N_s^k\left(\begin{array}{l}\frac{(1+\bar{\eta}_k)(1-\bar{\alpha}_k^2)}{(1-\bar{\alpha}_k^2\bar{I}_1^e)}\frac{(\bar{I}_1^e+2\bar{\eta}_k\bar{I}_2^e+3\bar{\eta}_k^2\bar{I}_3^e)}{(1+\bar{\eta}_k\bar{I}_1^e+\bar{\eta}_k^2\bar{I}_2^e+\bar{\eta}_k^3\bar{I}_3^e)}\\ +\ln[(1-\bar{\alpha}_k^2\bar{I}_1^e)(1+\bar{\eta}_k\bar{I}_1^e+\bar{\eta}_k^2\bar{I}_2^e+\bar{\eta}_k^3\bar{I}_3^e)]\end{array}\right)}_{w_s^k}\end{array}\right] \tag{24}$$

with

$$\begin{cases}\bar{I}_1^k=\mathrm{tr}(\bar{C}_k^e)\\ \bar{I}_2^k=\frac{1}{2}\left[\bar{I}_1^{k2}-\mathrm{trace}(\bar{C}_k^{e2})\right]\\ \bar{I}_3^k=\det(\bar{C}_k^e)\end{cases} \tag{25}$$

Note that in our case, $\bar{I}_3^k=\det(\bar{C}_k^e)=1$ so that the free energy is only a function of $(\bar{I}_1^k,\bar{I}_2^k)$.

The volumetric part of the free energy is chosen to follow the functional form of[39]

$$\hat{\bar{\psi}}_{J^e}(J^e)=\frac{1}{2}K_B\left[\frac{1}{2}(J^{e2}-1)-\ln J^e\right] \tag{26}$$

where K_B is an elastic bulk modulus. This functional form is introduced as a penalty function which approximately enforces the compressibility constraint of the material. In the following, N_s s and N_c will stand for $N_sk\theta$ and $N_ck\theta$, respectively, with k the Boltzmann's constant and θ, the absolute temperature and therefore are given in MPa.

The stress $\bar{S}$ in eq. (21), can therefore be written as

$$\begin{aligned}\bar{S}&=\sum_{k=1}^{2}(F_k^v)^{-1}\left(2\frac{\partial\bar{\psi}_v^k}{\partial\bar{C}_k^e}\right)(F_k^v)^{-T}\\ &=\sum_{k=1}^{2}(F_k^v)^{-1}\left(2\sum_{\bar{I}=1}^{2}\frac{\partial\bar{\psi}_v^k(\bar{I}_{\bar{I}}^k)}{\partial\bar{I}_{\bar{I}}^k}\frac{\partial\bar{I}_{\bar{I}}^k}{\partial\bar{C}_k^e}\right)(F_k^v)^{-T}\end{aligned} \tag{27}$$

with

$$\begin{cases}\frac{\partial\bar{I}_1^k}{\partial\bar{C}_k^e}=I\\ \frac{\partial\bar{I}_2^k}{\partial\bar{C}_k^e}=\bar{I}_1^kI-\bar{C}_k^e\end{cases} \tag{28}$$

and

$$p=\frac{1}{2}K_B(J-1/J) \tag{29}$$

The Cauchy stress in eq. (9) can then be computed by substituting eqs. (27) and (29) into eq. (20) as

$$\begin{aligned}\sigma&=J^{-1}\mathrm{FS}\mathrm{F}^T=J^{-1}[\mathrm{dev}(\bar{\mathrm{F}}\bar{\mathrm{S}}\bar{\mathrm{F}}^T)+p\mathrm{I}]\\ &=J^{-1}(\tau_{\mathrm{dev}}+\tau_{\mathrm{vol}})\end{aligned} \tag{30}$$

With

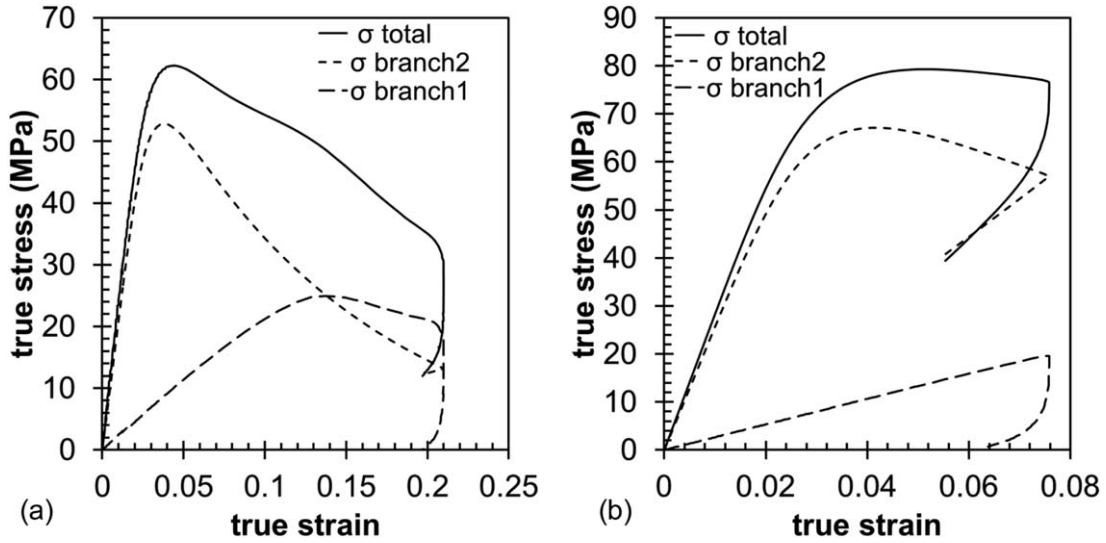

Figure 14. Contribution of chain interactions on stress-strain curves obtained for (a) amorphous PET and (b) semicrystalline PET.

$$\tau_{dev}=\sum_{k=1}^{2} 2\,\mathrm{dev}\left[\left(\frac{\partial\bar{\psi}_v^k}{\partial\bar{I}_I^k}+\frac{\partial\bar{\psi}_v^k}{\partial\bar{I}_2^k}\bar{I}_1^k\right)\bar{b}_k^e-\frac{\partial\bar{\psi}_v^k}{\partial\bar{I}_2^k}\bar{b}_k^{e2}\right] \tag{31}$$

$$\tau_{vol}=\frac{1}{2}K_B(J^2-1)\mathrm{I} \tag{32}$$

and

$$dev(\bullet)=(\bullet)-\frac{1}{3}[(\bullet):\mathrm{I}]\mathrm{I} \tag{33}$$

The terms $\frac{\partial\bar{\psi}_v^k}{\partial\bar{I}_1^k}$ and $\frac{\partial\bar{\psi}_v^k}{\partial\bar{I}_2^k}$ are defined in Appendix A.

Inelastic Flow Rules. To complement the constitutive description, the material viscous flow needs to be described to capture the kinetics of inelastic mechanisms observed during the deformation of the polymer.

In branch k, the velocity gradient of deformation, $\bar{D}_k^v$, can be expressed from φ_{int} in eq. (23)

$$\varphi_{int}=\bar{M}_k:\bar{D}_k^v-\left(\frac{\partial\bar{\psi}_v^k}{\partial\bar{\eta}_k}\dot{\bar{\eta}}_k+\frac{\partial\bar{\psi}_v^k}{\partial N_s^k}\dot{N}_s^k+\frac{\partial\bar{\psi}_v^k}{\partial\bar{\alpha}_k}\dot{\bar{\alpha}}_k\right)\geq 0\,,\quad k=\{1,2\} \tag{34}$$

Assuming that the internal work associated with the polymer network reorganization is proportional to the inelastic work, we have

$$\left(\frac{\partial\bar{\psi}_v^k}{\partial\bar{\eta}_k}\dot{\bar{\eta}}_k+\frac{\partial\bar{\psi}_v^k}{\partial N_s^k}\dot{N}_s^k+\frac{\partial\bar{\psi}_v^k}{\partial\bar{\alpha}_k}\dot{\bar{\alpha}}_k\right)=(1-\beta_k)\bar{M}_k:\bar{D}_k^v,\quad k=\{1,2\} \tag{35}$$

where β_k could be the coefficient of Taylor–Quinney.

Equation (34) is then given by

$$\begin{aligned}\varphi_{int}&=\bar{M}_k:\bar{D}_k^v-\left(\frac{\partial\bar{\psi}_v^k}{\partial\bar{\eta}_k}\dot{\bar{\eta}}_k+\frac{\partial\bar{\psi}_v^k}{\partial N_s^k}\dot{N}_s^k+\frac{\partial\bar{\psi}_v^k}{\partial\bar{\alpha}_k}\dot{\bar{\alpha}}_k\right)\\&=\bar{M}_k:\bar{D}_k^v-(1-\beta_k)\bar{M}_k:\bar{D}_k^{v}{}^{v}\qquad,\quad k=\{1,2\}\\&=\beta_k\bar{M}_k:\bar{D}_k^v\end{aligned} \tag{36}$$

The rate of inelastic deformation can be deduced from eqs. (34) and (36) as

$$\bar{D}_k^v=\frac{3}{2}\frac{1}{(1-\beta_k)}\frac{1}{|\mathrm{dev}(\bar{M}_k)|}\left(\frac{\partial\bar{\psi}_v^k}{\partial\bar{\eta}_k}\dot{\bar{\eta}}_k+\frac{\partial\bar{\psi}_v^k}{\partial N_s^k}\dot{N}_s^k+\frac{\partial\bar{\psi}_v^k}{\partial\bar{\alpha}_k}\dot{\bar{\alpha}}_k\right)\left(\frac{\mathrm{dev}(\bar{M}_k)}{|\mathrm{dev}(\bar{M}_k)|}\right),\quad k=\{1,2\} \tag{37}$$

where the Mandel stress,[43,44] $\bar{M}$, and the norm $|\bullet|$ can be expressed, respectively, as

$$\bar{M}=J^eR^{e-1}\sigma R^{e-T} \tag{38}$$

$$|\bullet|=\sqrt{\frac{3}{2}\bullet:\bullet} \tag{39}$$

The evolution equation for F_k^v is then represented by

$$\dot{F}_k^v=\bar{D}_k^vF_k^v,\quad \bar{D}_k^v=\dot{\bar{\gamma}}_k^v\bar{N}_k^v\quad k=\{1,2\} \tag{40}$$

where $\bar{N}_k^v=\mathrm{dev}(\bar{M}_k)/|\mathrm{dev}(\bar{M}_k)|$ is the direction of viscous flow, and $\dot{\bar{\gamma}}_k^v$ is a viscous shear strain rate. The terms $\frac{\partial\bar{\psi}_v^k}{\partial\bar{\eta}_k}$, $\frac{\partial\bar{\psi}_v^k}{\partial N_s^k}$, and $\frac{\partial\bar{\psi}_v^k}{\partial\bar{\alpha}_k}$ in eq. (37) is defined in Appendix A.

Microstructure Deformation Mechanisms

To finalize the description of the model, we need to describe the evolution of the microstructure for both contributions. Following Billon *et al.*,[1] the kinetics depends on elastic energy stored in the equivalent network. Thus, the more the elastic stored energy in network; the easier would be the rearrangement of this network. Moreover, the form of the below kinetic equations can reproduce different regimes at small and large deformations.

We define $\Delta\psi$ as the difference between the energy of the deformed polymer network and the undeformed one, that is, $\Delta\psi=\bar{\psi}_v^k(\bar{I}_1^k,\bar{I}_2^k,\bar{I}_3^k,\bar{\eta}_k,\bar{\alpha}_k)-\bar{\psi}_v^k(3,3,1,\bar{\eta}_k,\bar{\alpha}_k)$.

The evolution equation of $\bar{\eta}$ is related to the rate of chains slippage inducing a microstructure reorganization when submitted to an external loading. More especially, the variable $\bar{\eta}$ accounts for the disentanglement of the polymer chains. The evolution kinetics is assumed to be given by eq. (41)

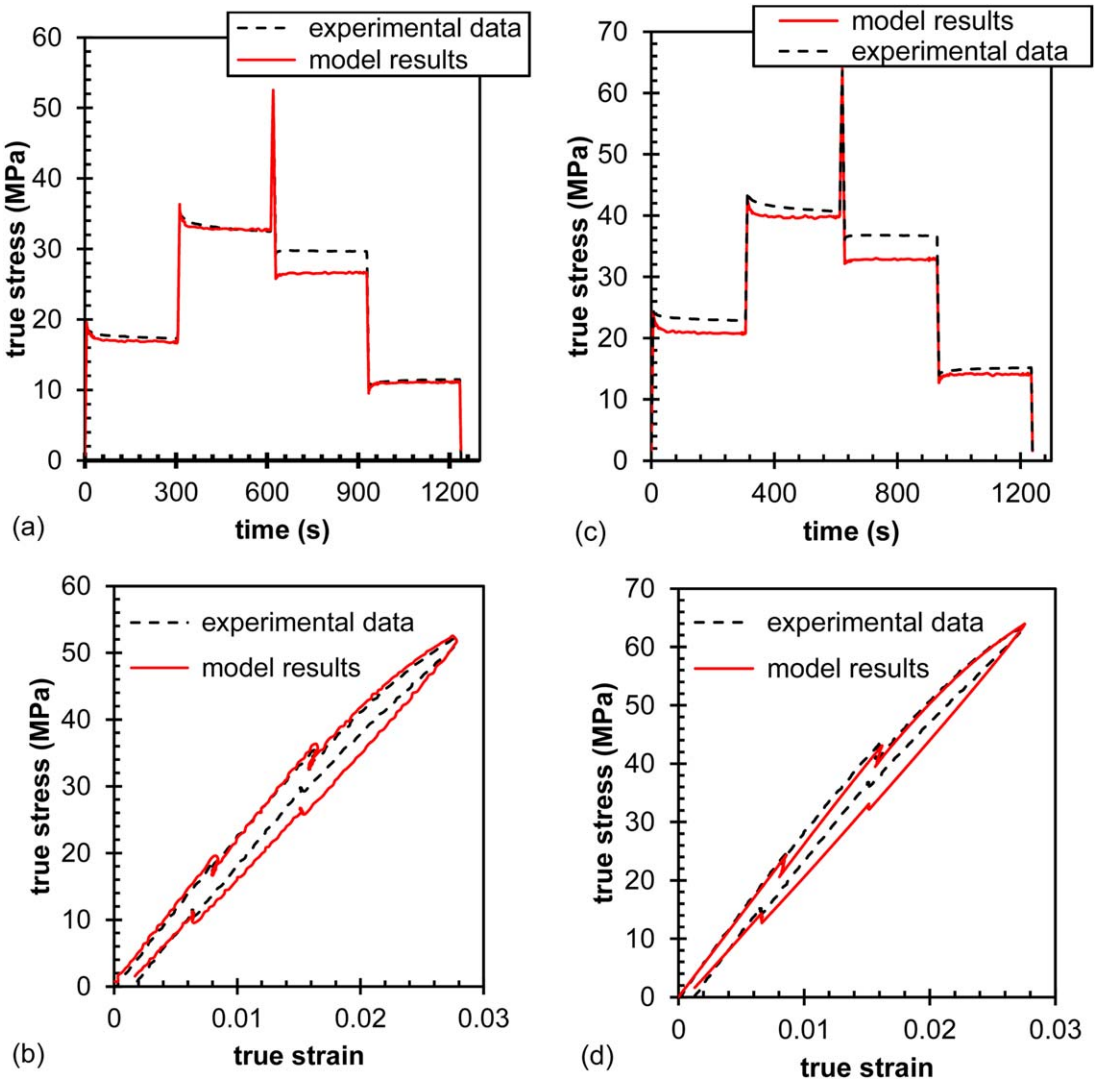

Figure 15. Comparison model-experimental for complex loading for amorphous PET (a) time-stress curves (b) strain-stress curve and for semicrystalline PET (a) time-stress curves (b) strain-stress curve. [Color figure can be viewed in the online issue, which is available at wileyonlinelibrary.com.]

$$\text{For } k=1, \dot{\eta} = \frac{Z \cdot \Delta\psi^{p_1}}{1+\tau \cdot \Delta\psi^{p_2}} \text{ and } \eta_0 = 0.2343$$
$$\text{For } k=2, \dot{\eta} = 0 \text{ and } \eta_0 = 0 \tag{41}$$

where Z, τ, p_1, and p_2 are material parameters.

The evolution equation of N_s^k is related to the modification of the weak bonds density. We postulated that an equilibrium value exists ($N_s^{\lim}$) depending on the amount of available energy $\Delta\psi$. A rate is therefore defined to reach this equilibrium according to eq. (42)

For $k=1$,

$$\dot{N}_s = 0$$

For $k=2$,

$$N_s^{\lim} = \frac{N_S^1}{1+(\tau_s \Delta\psi)^{\xi}}$$

$$\begin{cases} N_s^{\lim} - N_s > 0 \text{ then } \dot{N}_s = \upsilon |N_s^{\lim} - N_s|^p \\ N_s^{\lim} - N_s \leq 0 \text{ then } \dot{N}_s = -\upsilon' |N_s^{\lim} - N_s|^p \end{cases} \tag{42}$$

where υ, υ', p are material parameters.

The evolution equation of $\bar{\alpha}_k$ is related to alteration of chain extensibility. As already mentioned, the chains extensibility depends on the number of chain interaction points. Therefore, this kinetic of evolution needs to be proportional to the kinetic of evolution of N_s^k according eq. (43).

$$\text{For } k=1, \dot{\bar{\alpha}} = 0$$
$$\text{For } k=2, \dot{\bar{\alpha}} = \frac{\bar{\alpha}}{N_s} \dot{N}_s \tag{43}$$

All above kinetics could be viewed as phenomenological approach to describe microstructure's alteration.

Summary. Time effect in the present model is derived from the evolution of the internal variables linked to the polymer

Table I. Model Parameters for Each Microstructure

	Model parameter	Semicrystalline PET	Amorphous PET
Branch $k=1$	N_s (MPa/mm^3)	30.8	125.3
	N_c (MPa/mm^3)	67.7	$1.18{\cdot}10^{-4}$
	α^2 (·)	$1.07{\cdot}10^{-6}$	$1.08{\cdot}10^{-6}$
	β^a (·)	0	0
	Z (·)	323	350
	τ (·)	0.918	0.650
	$p1$ (·)	2.72	2.64
	$p2$ (·)	$1.15{\cdot}10^{-5}$	$1.15{\cdot}10^{-5}$
Branch $k=2$	N_s (MPa/mm^3)	63.3	54.5
	$N_c{}^a$ (MPa/mm^3)	0	0
	α^2 (·)	0.258	0.256
	β^a(·)	0	0
	τ_s (·)	6.37	8.25
	ξ (·)	2.13	2.35
	ν (·)	$3.02{\cdot}10^{-10}$	$3.01{\cdot}10^{-10}$
	ν' (·)	207	172
	p^a (·)	2	2

[a] Nonoptimized parameters.

microstructure. The energy needed for microstructures changes is balanced by elastic release and by dissipative effects. Microstructures changes are based on chains mobility and interactions. Inelastic processes are due to disentanglements and to the decrease of active weak bonds. In the case of uniaxial tensile loading, the behavior of each branch of the model is presented in Figure 12. We can notice that the first branch of the model characterized by the internal variable, η, reproduces a "viscoplastic-like" or long term viscoelastic-like behavior of the polymer induced by the "cooperative motion" of the polymer chains. The second branch characterized by the internal variables, N_s and α, represents a "viscoelastic-like" behavior of the material.

Uploading–unloading experimental investigations have shown an increase in temperature up to 5 °C, and the above constitutive model should be combined with some temperature dependence.[2] However, at this step, only the effect of crystallization was of first interest and according to Figure 3 and DMA analyses an increase of 5 °C close to 23 °C should not modify drastically the behavior of the two materials as they are in their glassy state. Therefore, material self-heating was neglected in this first investigation but integration of such thermomechanical coupling is important and will be considered in future works. One route to take thermal coupling into account is to use an extended multiplicative decomposition of the total deformation gradient F into nonlinear elastic F^e, inelastic F^v and isotropic thermal due to thermal expansion F^θ, see for instance.[44–47]

COMPARISON MODEL—EXPERIMENT

The constitutive model, described in the previous section, was validated under complex loading at different strain rates for both polymers, that is, amorphous PET and semicrystalline PET. However, the purpose of this study is not only to see the capabilities of such model to capture the mechanical behavior of the two polymers. Our focus is also to investigate the direct influence of the different mechanical behavior induced by the amorphous or the semicrystalline microstructure on the evolution of internal variables to assess their physical meaning.

Stress computations were performed by accounting for the local true strain rate that was experimentally measured (see for instance Figure 5). Model parameters for each microstructure were identified using inverse analysis on the whole set of uploading–unloading experimental data (Figure 13) and complex relaxation tests (Figure 15). Cost function was defined in a classical mean square method based on experimental and calculated equivalent stresses. Minimizations were conducted by means of the simplex algorithm of the "fminsearch" MATLAB® function. The identification procedure is able to find a set of parameters that reproduced experimental data with reasonable agreement for both materials. The model described in the section called constitutive modeling captured tensile cyclic loading performed at different strain rates (Figure 13) as well as relaxation loading (Figure 15) on amorphous and semicrystalline PET. Nevertheless, an underestimated stress was found in amorphous PET at high strain rate [Figure 13(b)]. The loss of precision was found to start with necking propagation.

The contribution of each branch on total stress is plotted on Figure 14. According to this figure, the polymer chains disentanglement appeared to be higher in amorphous network than in semicrystalline one. Moreover the weak bond arrangement in semicristalline PET lead to higher stress in branch 2.

The sets of parameters obtained by identification procedure for amorphous PET and semicrystalline PET is able to well describe

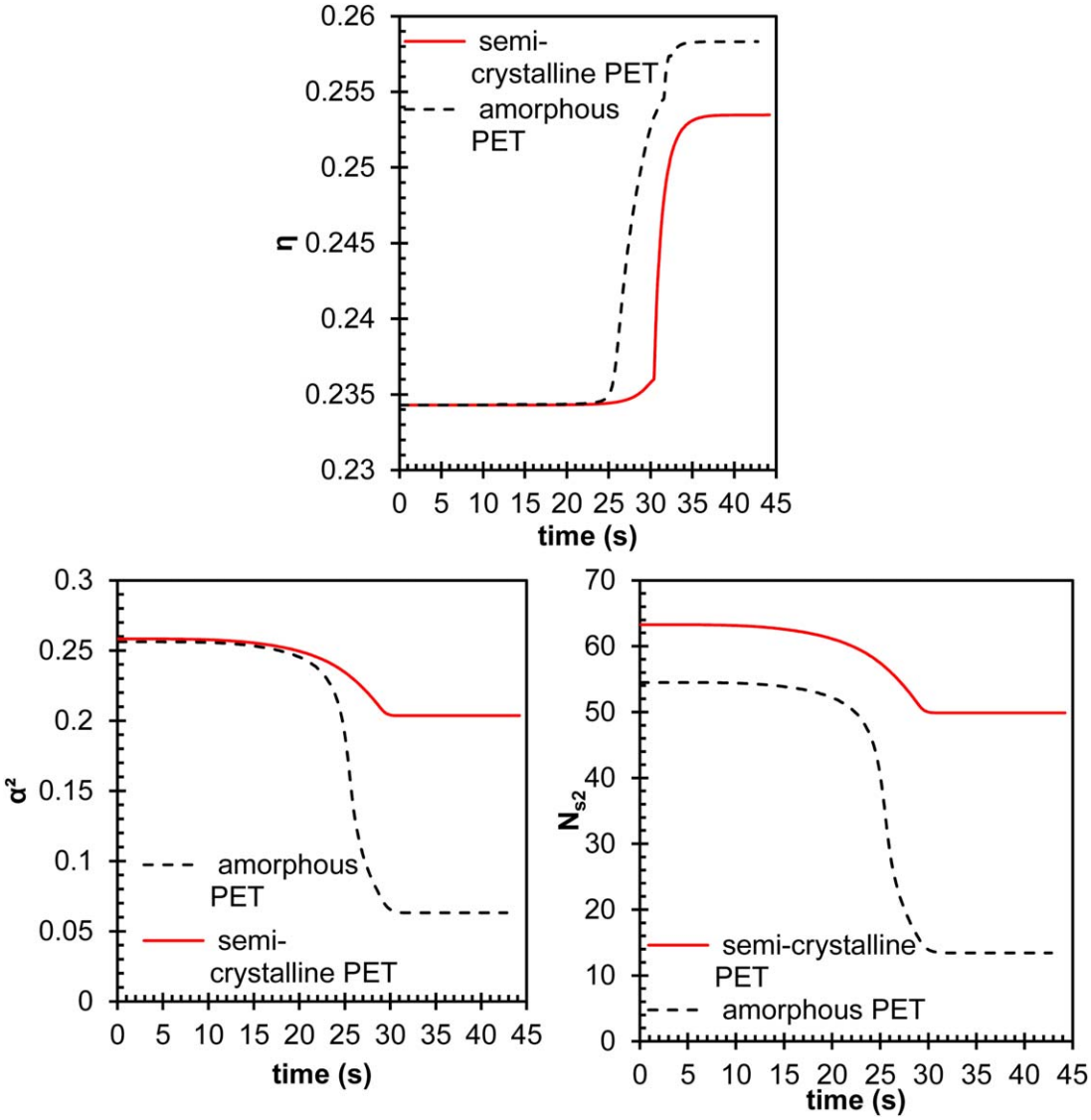

Figure 16. Evolution of model parameter linked to microstructure rearrangement during uploading-unloading tensile test at initial strain rate of $2 \cdot 10^{-3} s^{-1}$. [Color figure can be viewed in the online issue, which is available at wileyonlinelibrary.com.]

complex behavior of such materials (Figure 15). The several relaxation phases during loading are well captured with the model in both materials. Moreover on Figure 15, the experimental data showed an increase in stress during the relaxation steps when materials are unloaded this feature was also reported by refs. 48 and [49] and modeled by for instance.[50,51] Shape evolution of relaxation curves was called "anomalous" or "unusual"[52] behavior after strain reversal. Despite the facts that an underestimated stress was found in both materials, the proposed model captured this phenomenon sometimes called "anti-relaxation."

As mentioned earlier, the major goal of this work was to show how the described model built on chain network theory can capture the main characteristics of an amorphous and/or a semicrystalline network. As the microstructure affects the thermomechanical behavior of PET, the value of the model parameters should evolve with the microstructure. Due to the strong interaction between all the parameters, the impact of microstructure on the model parameters is not trivial. Thus, starting from a set of parameters that reasonably match the behavior of the amorphous PET, the inverse method was applied to the semicrystalline PET and parameters evolutions are analyzed. Values of the model parameters for each microstructures obtained by inverse methods are given in Table I.

In our formalism, equivalent polymer network is described by chain interactions; the chains are therefore linked by permanent nodes (N_c in branch 1) and/or slip-links (N_s in branch 1). As crystallization increase the connectivity in polymers, the crosslink node density (N_c in branch 1) is expected to be higher in semicrystalline PET than in amorphous PET. On contrary, the slip-link node density (N_s in branch 1) should be lower. In agreement with these observations, the identification of the semicrystalline PET led to higher crosslink density and lower slip-link density. Indeed, the permanent nodes density obtained for amorphous PET was close to 0 MPa and increased to 60

MPa for semicrystalline PET and slip-links node density dropped from around 125 MPa to almost 31 MPa (Table I).

The parameter η is related to the degree of mobility of chains in links. A zero η-value corresponds to permanent nodes. The model parameters Z, τ, $p1$, and $p2$ contribute to the evolution of the degree of mobility, η. Thus, the disentanglement is expected to decrease in the semicrystalline PET, due to the decrease of chain mobility induced by the presence of crystalline region. Therefore, the value of η should decrease. The latter remarks are in accordance with the model parameters obtained for each microstructure (Table I) which led to a higher mobility in amorphous PET. In fact, the value of η for semicrystalline PET subjected to external loading is lower than for the amorphous one (Figure 16).

The evolution equation of N_{s2} (in branch 2) is related to the evolution of weak bonds density and is associated to the viscoelastic mechanisms of the polymer under deformation. These links act as crosslink at small energy and disappeared as the energy increases. Thus, as the mobility and disentanglement are higher in amorphous PET, the decrease of weak bonds (N_{s2}) should be slower in semicrystalline PET. These observations are in agreement with value given in Table I and Figure 16 where the initial value of N_{s2} is higher for semicrystalline PET than for amorphous one.

The evolution equation of α^2 depends directly on the density of entanglement in the polymer chain network. For the semicrystalline PET, crystallization should result in an increase in α^2, which means that chains are less extensible.

CONCLUSIONS

The purpose of this work was to study the ability of a model built on chain network theory for capturing the main characteristics of an amorphous and a semicrystalline network. The thermomechanical constitutive model, based on the approach proposed by[1] and extended to 3D constitutive equations consistent with thermodynamic framework by Ref. 2 was enriched in terms of chain interactions and kinetic laws. The inelasticity of the polymer network was modeled through disentanglement mechanisms associated to the increase in the slippage length (η) and the evolution of weak bonds density (N_{s2}). This approach was validated for both amorphous and semicrystalline PET. The mechanical behavior of the two materials was investigated through nonmonotone tensile tests coupled with digital image correlation and temperature measurement using infrared camera to highlight the influence of the microstructure on the local behavior. Reasonable agreement was observed between model and experimental results. As expected the values of the physically motived internal variable are modified by the polymer microstructure. The study tended to confirm that permanent nodes could account for the crystalline contribution whereas the entanglements could account for the amorphous contributions. In the developed formalism, inelasticity arises from microstructure re-organization of the equivalent network, due to the presence of crystalline region in the polymer. Thus, the connectivity of the network is higher in the semicrystalline PET than in the amorphous one. The model showed its capability to capture this trend, as the evolution kinetics of the variables appears to be slower for the semicrystalline PET. In this first validation, the thermomechanical coupling was neglected but the integration of such coupling is important and will be considered in future works. Further investigations are needed to improve the kinetic laws as well as its implementation on a FE code to fully predict the mechanical behavior of the polymer.

APPENDIX A

$$\frac{\partial \bar{\psi}_v^k}{\partial \bar{I}_1^k}=\frac{1}{2}\left[\begin{array}{l} N_c^k\left(\frac{1-2\alpha_k^2-\alpha^4 I_1^k}{(1-\alpha_k^2\bar{I}_1^k)^2}\right) \\ +N_s^k\left(\begin{array}{l} -\frac{\alpha_k^2(1+\bar{\eta}_k)(1-\alpha_k^2)}{(1-\alpha_k^2\bar{I}_1^k)^2}\frac{\bar{I}_1^k+2\bar{\eta}_k\bar{I}_2^k+3\bar{\eta}_k^2\bar{I}_3^k}{1+\bar{\eta}_k\bar{I}_1^k+\bar{\eta}_k^2\bar{I}_2^k+\bar{\eta}_k^3\bar{I}_3^k} \\ +\frac{(1+\bar{\eta}_k)(1-\alpha_k^2)}{(1-\alpha_k^2\bar{I}_1^k)}\left(\frac{1-\bar{\eta}_k^2\bar{I}_2^k-2\bar{\eta}_k^3\bar{I}_3^k}{(1+\bar{\eta}_k\bar{I}_1^k+\bar{\eta}_k^2\bar{I}_2^k+\bar{\eta}_k^3\bar{I}_3^k)^2}\right) \\ +\frac{-\alpha_k^2}{1-\alpha_k^2\bar{I}_1^k}+\frac{\bar{\eta}_k}{1+\bar{\eta}_k\bar{I}_1^k+\bar{\eta}_k^2\bar{I}_2^k+\bar{\eta}_k^3\bar{I}_3^k} \end{array}\right) \end{array}\right] \tag{A.1}$$

$$\frac{\partial \bar{\psi}_v^k}{\partial \bar{I}_2^k}=\frac{1}{2}N_s^k\left(\begin{array}{l} \frac{(1+\bar{\eta}_k)(1-\alpha_k^2)}{(1-\alpha_k^2\bar{I}_1^k)}\left(\frac{2\bar{\eta}_k(1+\bar{\eta}_k\bar{I}_1^k+\bar{\eta}_k^2\bar{I}_2^k+\bar{\eta}_k^3\bar{I}_3^k)-\bar{\eta}_k^2}{(1+\bar{\eta}_k\bar{I}_1^k+\bar{\eta}_k^2\bar{I}_2^k+\bar{\eta}_k^3\bar{I}_3^k)^2}\right) \\ +\frac{\bar{\eta}_k^2}{(1+\bar{\eta}_k\bar{I}_1^k+\bar{\eta}_k^2\bar{I}_2^k+\bar{\eta}_k^3\bar{I}_3^k)} \end{array}\right) \tag{A.2}$$

$$\frac{\partial \bar{\psi}_v^k}{\partial \bar{\eta}_k}=\frac{1}{2}N_s^k\left(\begin{array}{l} \frac{(1-\alpha_k^2)((\bar{I}_1^k+2\bar{\eta}_k\bar{I}_2^k+3\bar{\eta}_k^2\bar{I}_3^k)+2(1+\bar{\eta}_k)(\bar{I}_2^k+3\bar{\eta}_k\bar{I}_3^k))}{(1-\alpha_k^2\bar{I}_1^k)(1+\bar{\eta}_k\bar{I}_1^k+\bar{\eta}_k^2\bar{I}_2^k+\bar{\eta}_k^3\bar{I}_3^k)} \\ -\frac{(1-\alpha_k^2)(1+\bar{\eta}_k)(\bar{I}_1^k+2\bar{\eta}_k\bar{I}_2^k+3\bar{\eta}_k^2\bar{I}_3^k)^2}{(1-\alpha_k^2\bar{I}_1^k)(1+\bar{\eta}_k\bar{I}_1^k+\bar{\eta}_k^2\bar{I}_2^k+\bar{\eta}_k^3\bar{I}_3^k)^2} \\ +\frac{(\bar{I}_1^k+2\bar{\eta}_k\bar{I}_2^k+3\bar{\eta}_k^2\bar{I}_3^k)}{(1+\bar{\eta}_k\bar{I}_1^k+\bar{\eta}_k^2\bar{I}_2^k+\bar{\eta}_k^3\bar{I}_3^k)} \end{array}\right) \tag{A.3}$$

$$\frac{\partial \bar{\psi}_v^k}{\partial N_s^k}=\frac{1}{2}\left(\begin{array}{l} \frac{(1-\alpha_k^2)(1+\bar{\eta}_k)(\bar{I}_1^k+2\bar{\eta}_k\bar{I}_2^k+3\bar{\eta}_k^2\bar{I}_3^k)}{(1-\alpha_k^2\bar{I}_1^k)(1+\bar{\eta}_k\bar{I}_1^k+\bar{\eta}_k^2\bar{I}_2^k+\bar{\eta}_k^3\bar{I}_3^k)} \\ +\log((1-\alpha_k^2\bar{I}_1^k)(1+\bar{\eta}_k\bar{I}_1^k+\bar{\eta}_k^2\bar{I}_2^k+\bar{\eta}_k^3\bar{I}_3^k)) \end{array}\right) \tag{A.4}$$

$$\frac{\partial \bar{\psi}_v^k}{\partial \bar{\alpha}_k}=\frac{1}{2}\left[\begin{array}{l} N_c^k\left(\bar{I}_1^k\frac{(\bar{I}_1^k-1)}{(1-\alpha_k^2\bar{I}_1^k)^2}-\frac{\bar{I}_1^k}{(1-\alpha_k^2\bar{I}_1^k)}\right) \\ +N_s^k\left(\frac{(1+\bar{\eta}_k)(\bar{I}_1^k+2\bar{\eta}_k\bar{I}_2^k+3\bar{\eta}_k^2\bar{I}_3^k)}{(1+\bar{\eta}_k\bar{I}_1^k+\bar{\eta}_k^2\bar{I}_2^k+\bar{\eta}_k^3\bar{I}_3^k)}\frac{(\bar{I}_1^k-1)}{(1-\alpha_k^2\bar{I}_1^k)^2}-\frac{\bar{I}_1^k}{(1-\alpha_k^2\bar{I}_1^k)}\right) \end{array}\right] \tag{A.5}$$

REFERENCES

1. Billon, N. *J. Appl. Polym. Sci.* **2012**, *125*, 4390.
2. Maurel-Pantel, A.; Baquet, E.; Bikard, J.; Bouvard, J. L.; Billon, N. *Int. J. Plast.* **2015**, *67*, 102. DOI: 10.1016/j.ijplas.2014.10.004.

3. Bouvard, J. L.; Ward, D. K.; Hossain, D.; Nouranian, S.; Marin, E. B.; Horstemeyer, M. F. *J. Eng. Mater. Technol.* **2009**, *131*, 041206. DOI: 10.1115/1.3183779.
4. Kennedy, M. A.; Peacock, A. J.; Mandelkern, L. *Macromolecules* **1994**, *27*, 5297. DOI: 10.1021/ma00097a009.
5. Tomita, Y.; Uchida, M. *Int. J. Mech. Sci.* **2005**, *47*, 687. DOI: 10.1016/j.ijmecsci.2004.10.011.
6. Ponçot, M.; Addiego, F.; Dahoun, A. *Int. J. Plast.* **2013**, *40*, 126. DOI: 10.1016/j.ijplas.2012.07.007.
7. Germain, P.; Nguyen, Q. S.; Suquet, P. *J. Appl. Mech.* **1983**, *50*, 1010.
8. Chaboche, J. *Int. J. Solids Struct.* **1997**, *34*, 2239.
9. Khan, A.; Farrokh, B. *Int. J. Plast.* **2006**, *22*, 1506. DOI: 10.1016/j.ijplas.2005.10.001.
10. Wei, P. J.; Chen, J. K. *Acta Mech.* **2003**, *164*, 217. DOI: 10.1007/s00707-002-1013-y.
11. Ayoub, G.; Zaïri, F.; Naït-Abdelaziz, M.; Gloaguen, J. M. *Int. J. Plast.* **2010**, *26*, 329. DOI: 10.1016/j.ijplas.2009.07.005.
12. Boyce, M. C.; Socrate, S.; Llana, P. G. *Polymer (Guildf)* **2000**, *41*, 2183. DOI: 10.1016/S0032-3861(99)00406-1.
13. Ahzi, S.; Makradi, A.; Gregory, R. V.; Edie, D. D. *Mech. Mater.* **2003**, *35*, 1139. DOI: 10.1016/S0167-6636(03)00004-8.
14. Shepherd, J.; Mcdowell, D.; Jacob, K. *J. Mech. Phys. Solids* **2006**, *54*, 467. DOI: 10.1016/j.jmps.2005.10.003.
15. Anand, L.; Ames, N. M.; Srivastava, V.; Chester, S. A. *Int. J. Plast.* **2009**, *25*, 1474. DOI: 10.1016/j.ijplas.2008.11.004.
16. Ames, N. M.; Srivastava, V.; Chester, S. A.; Anand, L. *Int. J. Plast.* **2009**, *25*, 1495. DOI: 10.1016/j.ijplas.2008.11.005.
17. Dusunceli, N.; Colak, O. U. *Int. J. Plast.* **2008**, *24*, 1224. DOI: 10.1016/j.ijplas.2007.09.003.
18. Krempl, E. Ho, K. In Time Dependent and Nonlinear Effects in Polymers and Composites; Schapery, R. A., Sun, C. T., Eds.; American Society for Testing and Materials Special Technical Publication: W. Conshohocken, PA, **2000**; Vol. *1357*, p 118.
19. Colak, O. U. *Int. J. Plast.* **2005**, *21*, 145. DOI: 10.1016/j.ijplas.2004.04.004.
20. Nikolov, S.; Doghri, I. *Polymer (Guildf)* **2000**, *41*, 1883. doi: 10.1016/S0032-3861(99)00330-4.
21. Bédoui, F.; Diani, J.; Régnier, G.; Seiler, W. *Acta Mater.* **2006**, *54*, 1513. DOI: 10.1016/j.actamat.2005.11.028.
22. Poluektov, M.; Van Dommelen, J. A. W.; Govaert, L. E.; Yakimets, I.; Geers, M. G. D. *J. Mater. Sci.* **2013**, *48*, 3769. DOI: 10.1007/s10853-013-7177-0.
23. Arnoult, M.; Dargent, E.; Mano, J. F. *Polymer (Guildf)* **2007**, *48*, 1012. DOI: 10.1016/j.polymer.2006.12.053.
24. Gueguen, O.; Ahzi, S.; Makradi, A.; Belouettar, S. *Mech Mater.* **2010**, *42*, 1. DOI: 10.1016/j.mechmat.2009.04.012.
25. Edwards, S. F.; Vilgis, T. *Polymer (Guildf)* **1986**, *27*, 483.
26. Ball, R.; Doi, M.; Eddwards, S.; Warner, M. *Polymer (Guildf)* **1981**, *22*, 1010.
27. Billon, N; Durin, A; Bouvard, J. The 9th International Conference on Mechanics of Time Dependent Materials Montreal, Canada, **2004**.
28. Vigier, G.; Tatibouet, J. *Polymer (Guildf)* **1993**, *34*, 4257.
29. Daubeny, R. de P.; Bunn, C. W. *Proc. R. Soc. A Math. Phys. Eng. Sci.* **1954**, *226*, 531. DOI: 10.1098/rspa.1954.0273.
30. Wunderlich, B. In *Crystal Melting*; Academic Press: New York, **1980**.
31. Schrauwen, B. Deformation and Failure of Semi-Crystalline Polymer Systems Influence of Micro and Molecular Structure, Technische Universiteit Eindhoven, **2003** Printed by the University Press Facilities, Eindhoven, the Netherlands ISBN-90-386-2914-1.
32. Flory, P. J. *Trans. Faraday Soc.* **1961**, *57*, 829.
33. Simo, J. C.; Taylor, R. L.; Pister, K. S. *Comput. Methods Appl. Mech. Eng.* **1985**, *51*, 177.
34. Lee, E. H. *ASME J. Appl. Mechanics* **1969**, *36*, 1.
35. Sidoroff, F. *J. Mec.* **1974**, *13*, 679.
36. Lubliner, J. *Mech. Res. Commun.* **1985**, *12*, 93.
37. Andriyana, A.; Silva, L.; Billon, N. *Appl. Mech. Mater.* **2010**, *24–25*, 419. DOI: 10.4028/www.scientific.net/AMM.24-25.419.
38. Maurel-Pantel, A.; Baquet, E.; Bikard, J.; Billon, N. *Appl. Mech. Mater.* **2011**, *70*, 393. DOI: 10.4028/www.scientific.net/AMM.70.393.
39. Simo, J. C.; Hughes, T. R. J. *Computational Inelasticity*; Springer-Verlag: New York, **1998**.
40. Reese, S.; Govindjee, S. *Int. J. Solids Struct.* **1998**, *35*, 3455.
41. Holzapfel, G. Nonlinear Solid Mechanics A continuum Approach for Engineering, **2000**, J. Wiley & Sons, Ltd., Chischester. ISBN 978-0-471-82319-3.
42. Coleman, B.; Gurtin, M. *J. Chem. Phys.* **1967**, *47*, 597.
43. Bouvard, J. L.; Ward, D. K.; Hossain, D.; Marin, E. B.; Bammann, D. J.; Horstemeyer, M. F. *Acta Mech.* **2010**, *213*, 71. DOI: 10.1007/s00707-010-0349-y.
44. Bouvard, J. L.; Francis, D. K.; Tschopp, M. A.; Marin, E. B.; Bammann, D. J.; Horstemeyer, M. F. *Int. J. Plast.* **2013**, *42*, 168. DOI: 10.1016/j.ijplas.2012.10.005.
45. Nguyen, T.; Jerryqi, H.; Castro, F.; Long, K. *J. Mech. Phys. Solids* **2008**, *56*, 2792. DOI: 10.1016/j.jmps.2008.04.007.
46. Francis, D. K.; Bouvard, J. L.; Hammi, Y.; Horstemeyer, M. F. *Int. J. Solids Struct.* **2014**, *51*, 2765. DOI: 10.1016/j.ijsolstr.2014.03.025.
47. Ge, Q.; Luo, X.; Iversen, C. B.; Nejed, H. B.; Mather, P. T.; Dunn, M. L.; Qi, H. J. *Int. J. Solids Struct.* **2014**, *51*, 2777. DOI: 10.1016/j.ijsolstr.2014.03.029.
48. Zhang, C.; Moore, I. *Polym. Eng. Sci.* **1997**, *37*, 404.
49. Khan, F. *J. Eng. Mater. Technol. ASME* **2006**, *128*, 564. SI) DOI: 10.1115/1.2345448.
50. Drozdov, A. D. *Math. Comput. Model.* **1998**, *27*, 45. DOI: 10.1016/S0895-7177(98)00072-7.
51. Drozdov, A. D. *Int. J. Solids Struct.* **2010**, *47*, 3221. DOI: 10.1016/j.ijsolstr.2010.08.001.
52. Heymans, N.; Kitagawa, M. *Rheol. Acta* **2004**, *43*, 383. DOI: 10.1007/s00397-003-0354-3.